Combining gravitational wave search pipelines to find subthreshold signals in GWTC-5.0

Ann-Kristin Malz,[1,*] Samuel Russell,[1] Gregory Ashton,[1,2] and Nicolo Colombo[3]

[1] *Department of Physics, Royal Holloway, University of London*
[2] *School of Mathematical Sciences, University of Southampton*
[3] *Department of Computer Science, Royal Holloway University of London*

(Dated: July 23, 2026)

The detection of transient gravitational wave signals relies on independent search algorithms that analyse detector data and assign significance measures to candidate events. However, varying performance complicates their interpretation. We use supervised machine learning combined with conformal prediction, a framework to quantify uncertainties, to merge multi-pipeline information into well-calibrated confidence scores. We demonstrate that this approach is robust across different classifier architectures and remains stable when trained on different simulated datasets. When applied to events across the GWTC catalogue up to and including the second part of the fourth observing run, the framework identifies several subthreshold candidates with elevated confidence, including the binary neutron star candidate GW200311_103121. We examine the reliability of these up-rankings, finding evidence that high-confidence predictions correspond to signal-like events. This framework enables simplified systematic candidate assessment for gravitational wave catalogues and real-time alerts by providing a single, well-calibrated confidence measure per candidate.

arXiv:2607.07272v2 [gr-qc] 22 Jul 2026

I. INTRODUCTION

The field of gravitational wave (GW) astronomy is rapidly expanding with the growing number of detections. With the latest data release, GWTC-5.0 [1], the cumulative catalogue of events now contains almost 400 signals generated by compact binary coalescences (CBCs) and observed by the LIGO-Virgo-KAGRA (LVK) detectors [2–4]. The majority of these signals are caused by binary black hole (BBH) mergers, with a small number of neutron star black hole (NSBH) and only two binary neutron star (BNS) detections. BNS signals are of particular interest because they can produce electromagnetic counterparts that enable multi-messenger astronomy [5], allowing for independent measurements of cosmological parameters [6] and providing crucial insights into the properties of ultra-dense matter [7].

GW signals are extracted from noisy detector data [8] using advanced search algorithms (pipelines), which assign a false alarm rate (FAR) to each candidate by comparing its detection statistic against an estimated background [9]. The pipeline outputs can then be combined with an astrophysical model to calculate a Bayesian $p_{\rm astro}$ [10], which quantifies the probability that the candidate is an astrophysical signal [1].

Within the LVK collaboration, multiple search pipelines are currently routinely used, providing complementary sensitivity and improved robustness. Four of them (`GstLAL` [11–17], `MBTA` [18–20], `PyCBC` [21–26], and `SPIIR` [27, 28]) rely on matched filtering, where models of CBC signals are used, while `cWB` [29–34] performs an unmodelled, coherence-based search. Additional information is detailed in Abac et al. [9]. There are also several other search pipelines, such as the machine learning (ML) based `Aframe` [35] and `MLy` [36] pipelines, as well as independent searches [37, 38].

The use of multiple pipelines creates challenges when their outputs for a particular candidate do not agree. This can arise from differences in search methodology, tuning, and configuration choices, as well as parameter-space-dependent sensitivities and varying susceptibility to noise artifacts. Combining these outputs into a single robust significance measure per candidate is therefore essential.

Currently, the maximum inverse false alarm rate (IFAR) across pipelines, where IFAR=1/FAR, is used to classify candidates as significant, and those with $p_{\rm astro} \geq 0.5$ from at least one pipeline are included in the gravitational wave transient catalogue (GWTC) as astrophysical signals [1, 39, 40]. This maximum across pipelines approach is straightforward and computationally efficient. Alternative methods have been explored, such as producing a unified $p_{\rm astro}$ [41].

Nevertheless, differing pipeline outputs carry additional information about the nature of a candidate. The maximum significance approach neglects this, as it only accounts for information from the most significant pipeline candidate. A signal, for instance, should be consistently detected across pipelines with compatible properties, whereas a noise artifact may only trigger a single pipeline sensitive to that particular noise type. By exploiting these correlations, we can therefore learn additional information about candidate events.

Several other ML classifier approaches have also been proposed (Tsukamoto et al. [42], Moustakidis et al. [43]) to learn such correlations and improve the characterisation of candidate events. Most ML algorithms produce uncalibrated predictions without associated uncertainties, yet reliable uncertainty quantification is essential when assessing whether a GW candidate is of astrophysical origin. In Ashton et al. [44], we therefore applied conformal

* ann-kristin.malz@ligo.org

prediction (CP) [45, 46] to quantify the uncertainties of the ML algorithm and provide well-calibrated conditional confidence scores for each candidate. The conditional confidence [47] is a score in $[0, 1]$ quantifying how signal-like a candidate appears.

The application of CP in astrophysics is recent but expanding, with work covering redshift estimation [48, 49], stellar spectra classification [50], black hole mass estimation [51], neutron star equation of state inference [52], and measurement error propagation [53], as well as work in high-energy physics [54] and a series of applications in gravitational-wave astronomy [44, 47, 55], including the line of work upon which the present work builds.

In Ashton et al. [44], we demonstrated that our method outperforms the maximum-$\log_{10}$IFAR approach on simulated data, achieving superior receiver operating characteristic (ROC) curves and area under the curve (AUC) scores. When applied to the catalogue from the third observing run, O3 [39, 56], our framework notably assigned a high confidence score to the subthreshold BNS candidate GW200311_103121.

We reproduce the key result of Ashton et al. [44] in Fig. 1, showing conditional confidence scores obtained by combining logistic regression (LR) with CP for GW candidates in the third observing run (O3). In the bottom-right quadrant, we find candidates with $p_{\rm astro} \geq 0.5$ but subthreshold (here 0.5, see Appendix B 3) conditional confidence. The majority of these candidates are single-pipeline events, mostly by `GstLAL` or `cWB`, including GW190425_081805, a single-detector BNS [56, 57]. In the top-left quadrant, we identify several candidates that fall below the $p_{\rm astro}$ threshold of 0.5 but with conditional confidence values above 0.5. In addition to the BNS candidate GW200311_103121 with a FAR just above threshold ($1.3\ {\rm yr}^{-1}$) in two pipelines, we identify the marginally significant NSBH candidates GW190426_152155, GW190531_023648, and GW200201_203549 [39] and several BBH events, each found by the `GstLAL`, `PyCBC`, and `MBTA` pipelines. A full list of conditional confidence scores and $p_{\rm astro}$ values for all events in these quadrants is included in Appendix C.

These results are promising, suggesting that several sub-threshold candidates may be of astrophysical origin. However, CP assumes exchangeability between the data used to calibrate the framework and the data it is applied to [58], which may not hold if there are changes to the search pipelines or detectors, raising the question of whether the conditional confidence scores shown in Fig. 1 are reliable. Addressing this requires both empirical robustness checks, confirming that results are stable across model and data choices, and physical validation that the classifiers learn meaningful signal properties rather than artefacts of the training data.

In this work, we extend and validate the framework of Ashton et al. [44]. Specifically, we apply our framework to new candidates from the fourth observing run, O4, in GWTC-4.1 and GWTC-5.0, while validating the reliability of these results by comparing different ML classifiers, investigating the features driving predictions, and assessing robustness using new mock data.

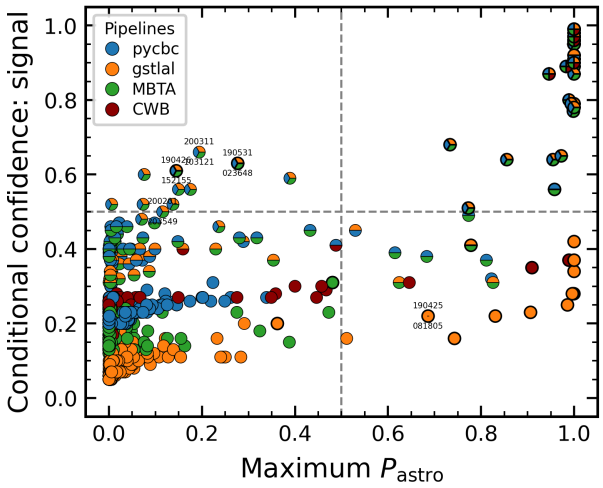


FIG. 1. The conditional confidence in the signal label for the LR classifier compared to the maximum $p_{\rm astro}$ for the O3 events in the combined GWTC-2.1 and GWTC-3.0 catalogues. The classifier is trained and CP calibrated on the MDC data. The dashed lines represent the conditional confidence and $p_{\rm astro}$ thresholds, respectively. The markers are coloured by the search pipelines which detected each candidate, and high-significance events (FAR < 1 per year) are indicated by a bold marker outline. We highlight names of candidates discussed in the text. The plot is reproduced from Fig. 3 of Ashton et al. [44], but due to a correction in the data assembling now includes several candidates that were previously mistakenly excluded.

The paper is structured as follows. In Section II, we outline the ML classifiers and CP framework used to combine pipeline outputs. In Section II A, we compare the performance of different classifier architectures and assess the robustness of the framework to the choice of classifier. In Section II B, we examine robustness with respect to training and calibration data, by exploring the use of two different mock data sets. Furthermore, by examining what events are up-ranked in the mock data and using the new mock data as an unseen test, we investigate the trustworthiness of the catalogue events to which we assign increased confidence. In Section III A and Section III B, we apply our framework to the new O4a and O4b candidates in the GWTC-4.1 and GWTC-5.0 catalogue, respectively, using parameter estimation and feature investigation to assess how signal-like the candidates with high conditional confidence are. Finally, we discuss our results and conclude in Section IV.

II. METHOD AND VALIDATION

We combine the search pipelines following the same approach as in Ashton et al. [44]: first using a ML binary

classifier to combine pipeline outputs, and second applying CP [45, 46] to quantify the uncertainty and obtain a well-calibrated conditional confidence score for each candidate.

The classifier takes as input a feature vector assembled from the outputs of the `cWB`, `PyCBC`, `GstLAL`, and `MBTA` pipelines, comprising per-pipeline detection statistics and, where available, source parameter estimates from the nearest waveform template. When applying our method to the new candidates in GWTC-2.1 [56, 59], GWTC-3.0 [39, 60], GWTC-4.1 [40, 61], and GWTC-5.0 [1, 62], we restrict the features to the $\log_{10}$(IFAR), signal-to-noise ratio (SNR), and chirp mass, setting the chirp mass to zero for `cWB`, which does not provide template-based parameter estimates (see Appendix A for details). Candidates not detected by a given pipeline are assigned feature values of zero, which for the $\log_{10}$(IFAR) is consistent with the absence of a reported IFAR. To train the ML classifiers and calibrate CP we mainly use the pre-O4 mock data challenge (MDC) [63], while the smaller low-latency production integration challenge (LLPIC) dataset [64] created during O4 is used for additional robustness tests in Section II B.

In Ashton et al. [44], we focused mainly on the logistic regression (LR) classifier due to its interpretability. In this work, we extend the comparison to multi-layer perceptron (MLP) [65] and XGBoost, a gradient-boosted tree ensemble [66]. The raw output from the ML classifiers lacks a statistically rigorous significance measure, unlike the FAR provided by the maximum-$\log_{10}$IFAR approach, an essential component for assessing the significance of individual candidate events. We therefore apply Mondrian (label-conditional) CP [67], which provides coverage guarantees separately for signals and noise events, to the ML classifier output to produce a *prediction set* of possible labels. However, GW candidate assessment requires a single score quantifying significance of each candidate, for which we use the *conditional confidence* [47]. The conditional confidence score provides a single well-calibrated significance measure per candidate: values close to one indicate strong support for the signal hypothesis, while values close to zero indicate noise-like behaviour.

Full details of the data preparation, classifier architectures, and CP formalism are given in Appendix A.

A. Robustness to classifier architecture

We compare the performance of the ML classifiers to assess whether the pipeline combination framework is effective and whether results are robust to the choice of classifier. We evaluate each classifier using ROC curves and sensitivity and precision metrics under CP, and examine consistency on real GW candidates from O3. Full details and figures are given in Appendix B.

We evaluate the ML classifiers on the MDC dataset, and present the resulting ROC curves in Fig. 2, alongside the maximum-$\log_{10}$IFAR approach for comparison. All ML classifiers outperform the maximum-$\log_{10}$IFAR method, demonstrating the benefit of exploiting correlations between pipeline outputs rather than relying on any single pipeline statistic. XGBoost achieves the highest AUC on the mock data, approximately one standard deviation above MLP and nearly five standard deviations above maximum-$\log_{10}$IFAR, suggesting that its non-linear, tree-based structure is particularly effective at capturing complex interactions between features, although all ML classifiers show a clear and systematic improvement over the maximum-$\log_{10}$IFAR method. XGBoost also leads on the precision and sensitivity metrics, see Appendix B 2. At a conditional confidence threshold of 0.5 (see Appendix B 3 for the threshold justification), LR and XGBoost produce zero false positives on the MDC data, compared to one for MLP and maximum-$\log_{10}$IFAR.

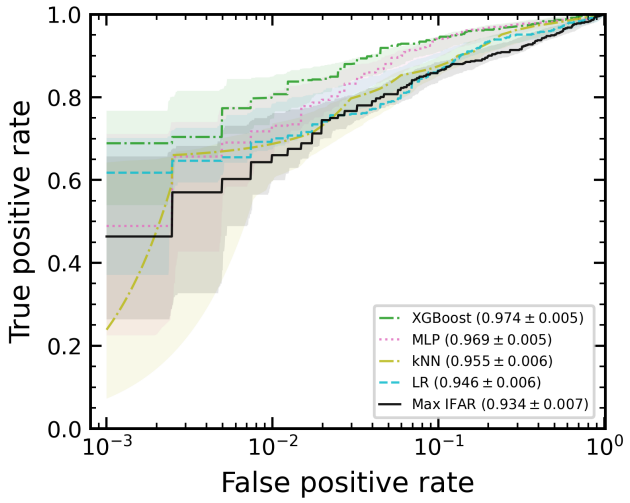


FIG. 2. ROC curve comparing the performance of four different ML classifiers and the maximum-$\log_{10}$IFAR method on the MDC dataset. The shaded band marks the 90% interval over 100 random permutations of the training and testing data. The AUC is given in the legend for each classifier, including the standard deviation obtained from the train-test data split permutations.

Applied to the O3 candidates from GWTC-2.1 and GWTC-3.0, all three classifiers show broad agreement. In particular, the sub-threshold BNS candidate GW200311_103121 listed in the marginal candidate table of GWTC-3.0, and the two GWTC-2.1 marginal significance NSBH candidates GW190426_152155 and GW190531_023648, are consistently assigned above-threshold confidence by all classifiers, lending additional support to their potential astrophysical origin. XGBoost is the most conservative classifier, up-ranking only events with strong multi-pipeline support, while MLP is the least conservative, also up-ranking single- and two-pipeline candidates. The conservative behaviour is preferred: false positives, noise events misidentified as astrophysical signals, carry a higher cost than false negatives in GW

astronomy.

The broad agreement across classifiers demonstrates that the framework is robust to the choice of classifier architecture, with differences arising primarily in the degree of conservatism. Based on its superior AUC, near-zero false positive rate, and conservative behaviour on real candidates, we identify XGBoost as our preferred classifier for the remainder of this analysis.

To understand what drives individual predictions, we perform a SHapley Additive exPlanations (SHAP) analysis [68], which confirms that the classifiers learn physically meaningful patterns: $\log_{10}$(IFAR) features from the templated pipelines dominate, with higher values pushing toward a signal prediction, while missing detections in sensitive pipelines push toward a noise prediction. See Appendix B 4 for full details and plots.

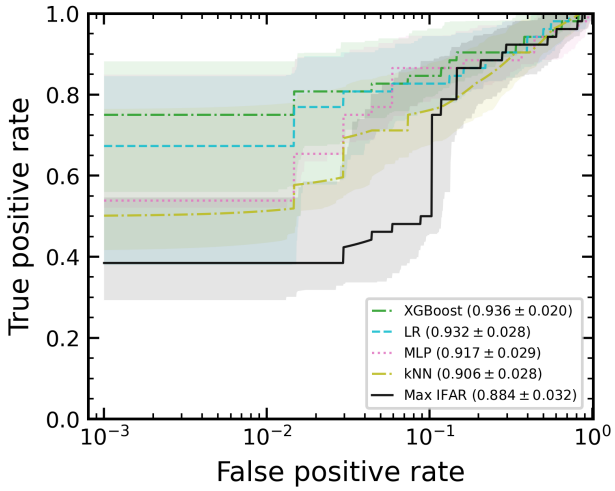


FIG. 3. ROC curves comparing the performance of four different ML classifiers and the maximum-$\log_{10}$IFAR method as trained, calibrated and tested on the LLPIC dataset. The shaded band marks the 90% interval over the permutations of the training and testing data. The AUC is given in the legend for each classifier, including the uncertainty over train-test data split permutations.

B. Robustness to training and calibration data

Having established our framework on the MDC data, we now turn to the more recent LLPIC datasets, as described in Appendix A 1, to assess its robustness. As discussed in Section I, the exchangeability assumption underpinning CP cannot be strictly guaranteed in practice. Since the MDC and LLPIC are based on data from different observing runs and therefore reflect differences in detector configuration and pipeline implementations (see Abac et al. [9] for details), using the LLPIC provides a direct probe of this assumption.

We use this new dataset in two ways: first, as a consistency check to assess whether we obtain results consistent with those from the MDC dataset; and second, as independent test data to evaluate whether the conditional confidence can be trusted where it disagrees with the maximum-$\log_{10}$IFAR classification.

1. *Consistency check with LLPIC*

We begin by training, calibrating, and testing our framework on the LLPIC dataset, and mirror the analysis performed on the MDC data, thus checking the consistency and robustness of our method.

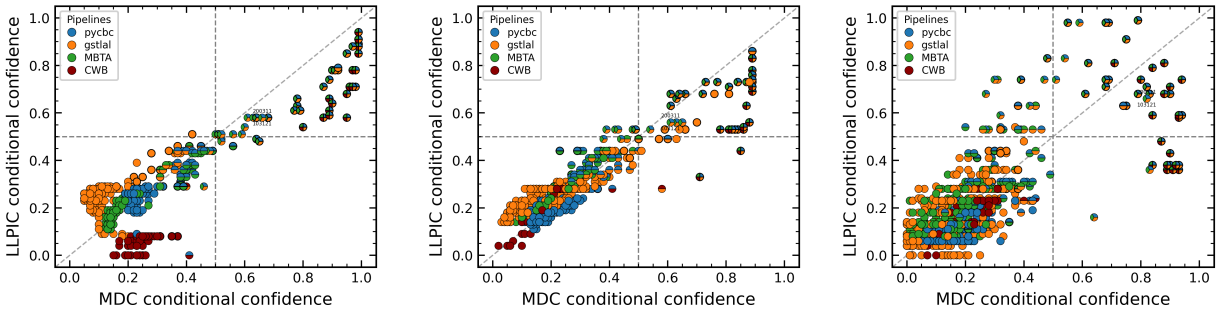
We assess the performance of the different classifiers using the ROC curve shown in Fig. 3, observing consistent results compared to the MDC: all ML classifiers outperform the maximum-$\log_{10}$IFAR combination method, with XGBoost achieving the highest AUC. At a conditional confidence threshold of 0.5, no false positives are produced and approximately 50% of signals are recovered by all classifiers and the maximum-$\log_{10}$IFAR. This confirms that the framework generalises to the LLPIC dataset and that the result is not dependent on the training dataset used.

Next, we calculate the conditional confidence for the O3 events in the GWTC-2.1 and GWTC-3.0 catalogues, using LLPIC as training and calibration data. To highlight the comparison with the MDC-trained framework, the confidences as obtained from each of the different training datasets are plotted against each other in Fig. 4.

The LLPIC dataset is significantly smaller than the MDC, which affects classifier performance. While simple models such as LR are generally more robust with limited data due to their lower complexity, more flexible models such as XGBoost may require more training data to generalise reliably [66, 69].

The plots for LR and MLP, in Fig. 4(a) and Fig. 4(b) respectively, show good agreement between confidences for most events. For XGBoost (Fig. 4(c)), the conditional confidence values show greater variations between the two datasets, suggesting this classifier is more sensitive to the choice of training data. While LR and MLP give generally lower confidence when trained and calibrated on the LLPIC data, for XGBoost more events are above the confidence threshold with this dataset. For all classifiers we observe that the BNS candidate GW200311_103121 and the two NSBH candidates GW190426_152155 and GW190531_023648 have confidence values above the threshold regardless of training data.

From this investigation, we conclude that our results remain broadly consistent when switching the training and calibration data despite the smaller size of the LLPIC, supporting the robustness of the framework. Although exchangeability cannot be guaranteed for the LLPIC data either, the consistency across classifiers suggests our approach is reasonably tolerant to the choice of training and calibration dataset. The exception is XGBoost, which shows greater sensitivity to this choice, consistent with



(a) LR (b) MLP (c) XGBoost

FIG. 4. The conditional confidence in the signal label for the O3 events in the GWTC-2.1 and GWTC-3.0 catalogue as obtained from training and calibration on the MDC versus LLPIC data respectively. The dashed lines represent the conditional confidence threshold at 0.5. Events with maximum-$p_{\rm astro}$ above 0.5 are indicated by a bold marker outline.

its higher model variance discussed in Appendix B 1.

2. *Using LLPIC as unseen test data*

Next, we assess whether the up- and down-rankings produced by our framework can be trusted when exchangeability is broken. For this purpose, we train and calibrate our framework on the MDC data, as before, and use LLPIC as independent test data, mimicking the distribution shift between mock and real data. This allows us to examine whether events assigned high conditional confidence despite low maximum-$\log_{10}$IFAR genuinely appear signal-like, and whether events down-ranked despite high maximum-$\log_{10}$IFAR appear noise-like.

Fig. 5 shows the conditional confidence scores for the LLPIC test events (as trained and calibrated on the MDC data) plotted against the maximum-$\log_{10}$IFAR. For the majority of events, the two methods are in agreement for both the LR and XGBoost classifiers, though XGBoost shows greater scatter.

Investigating the quadrants where the two methods disagree, we find that all candidates up-ranked by our framework correspond to signals, except for one noise candidate located on the threshold for XGBoost and at conditional confidence of 0.6 for LR. There are several noise candidates that have been incorrectly classified as signals by the maximum-$\log_{10}$IFAR method, but which are classified as noise by both classifiers. However, there are also several signals that our framework down-ranks.

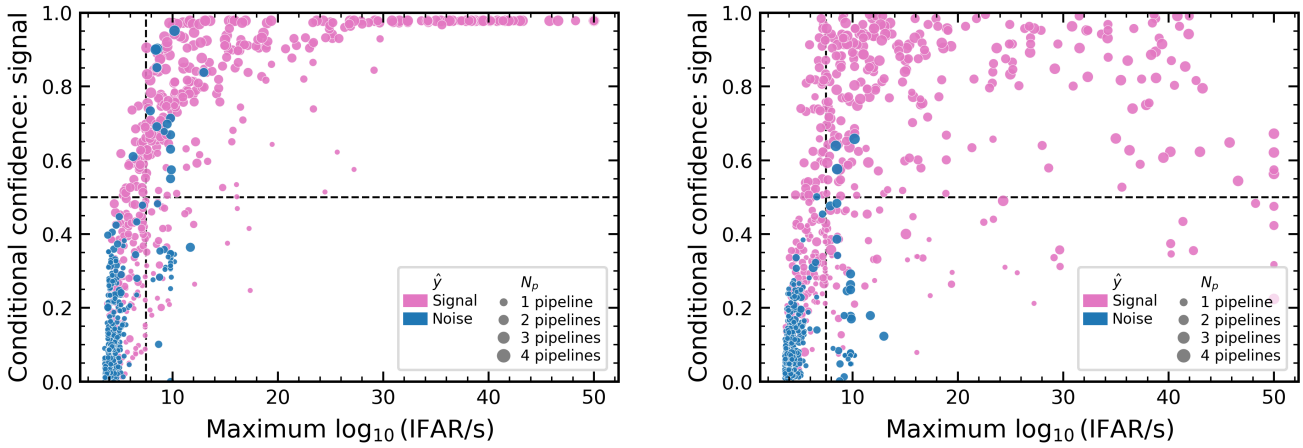
While XGBoost returns fewer false positives than LR, there are also significantly more high maximum-$\log_{10}$IFAR signal events with sub-threshold conditional confidence. This broader spread in XGBoost confidences was also apparent in the MDC results (see Fig. 13). However, using different datasets for training and calibration versus testing, this effect appears to become more pronounced, leading XGBoost to down-rank a substantially larger number of high-maximum-$\log_{10}$IFAR, multi-pipeline signals. Thus, while XGBoost's up-rankings appear reliable, its down-rankings warrant caution. LR demonstrates more balanced behaviour, down-ranking primarily marginal candidates near the detection threshold and single-pipeline detections.

TABLE I. Performance of the different classifiers + CP and the maximum-$\log_{10}$IFAR method trained and calibrated on the MDC and tested on the LLPIC dataset. A threshold of 0.5 on the conditional confidence is applied for the ML classifiers and a FAR of 1 per year for the maximum-$\log_{10}$IFAR.

Method	TP	FP	FN	TN
LR	316	15	217	655
XGBoost	287	4	246	666
MLP	334	18	199	652
max $\log_{10}$(IFAR)	305	51	228	619

We quantify the observations from Fig. 5 in Table I, using the same conditional confidence and maximum-$\log_{10}$IFAR thresholds as before, see Section II A. All three ML classifiers produce far fewer false positives than the maximum-$\log_{10}$IFAR method (LR: 15, XGBoost: 4, MLP: 18, versus 51 for maximum-$\log_{10}$IFAR), demonstrating a clear advantage in noise rejection. XGBoost is the most conservative, achieving the fewest false positives (0.6%) but also the lowest true positive rate (53.8%). MLP recovers the most signals (62.7%) at the cost of slightly more false positives (2.7%), while LR offers an intermediate balance (59.3% TPR, 2.2% FPR). The higher false positive rate of maximum-$\log_{10}$IFAR (7.6%) likely reflects differences in noise characteristics between the LLPIC data and the assumptions underlying the FAR threshold. We further observe that nearly all noise events incorrectly classified as signals by the conditional confidence also have maximum-$\log_{10}$IFAR values above threshold, suggesting these are borderline cases where both methods struggle. Meanwhile, many noise candidates defined as signals by the maximum-$\log_{10}$IFAR method have very small conditional confidence values.

Having validated the framework's general performance,



(a) LR

(b) XGBoost

FIG. 5. The conditional confidence in the signal label for the LR (left) and XGBoost (right) classifiers, respectively, compared to the maximum IFAR, using training and calibration data from the MDC and testing on LLPIC. The dashed lines show the chosen conditional confidence threshold of 0.5 and the commonly used FAR threshold of 1 per year. The colour of each point indicates the true label $\hat{y}$, while the size indicates the number of pipelines N_p which detected an event.

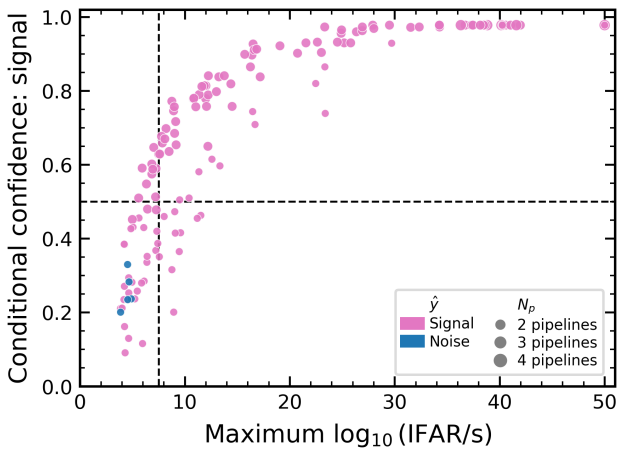


FIG. 6. The conditional confidence in the signal label for the LR classifier compared to the maximum IFAR, using training and calibration data from MDC and testing on LLPIC, showing only BNS injections ($M_1 \leq 3$) recovered by at least two pipelines for clarity. The dashed lines show the chosen conditional confidence threshold of 0.5 and the commonly used FAR threshold of 1 per year. The colour of each point indicates the true label $\hat{y}$, while the size indicates the number of pipelines N_p which detected an event.

we now focus on whether it correctly identifies BNS-like injections, motivated by the up-ranked BNS candidate GW200311_103121 from GWTC-3.0. To obtain an estimate of the performance of our framework on similar events in the LLPIC data, we plot the conditional confidence for BNS events only (limiting the source frame component masses at $\leq 3M_\odot$ to select signals consistent with neutron stars) in Fig. 6.

Among the three-pipeline BNS injections, only three obtain a conditional confidence below threshold, all of which were classified as noise by the maximum-$\log_{10}$IFAR. This confirms that sub-threshold BNS candidates with multi-pipeline detections, analogous to GW200311_103121, are correctly identified as signals by our framework even under distribution shift.

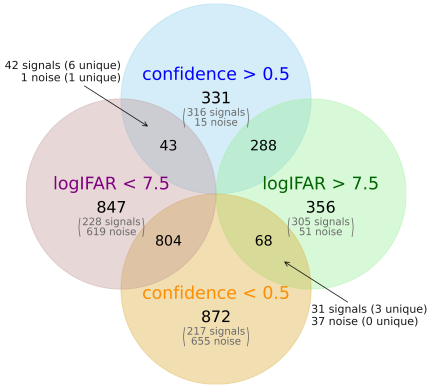
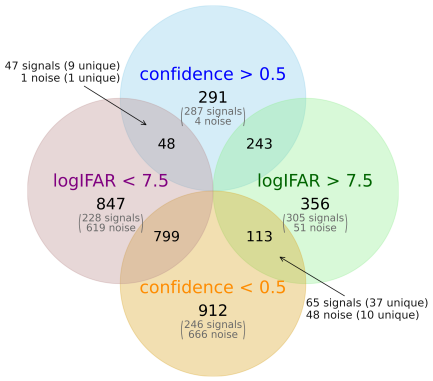
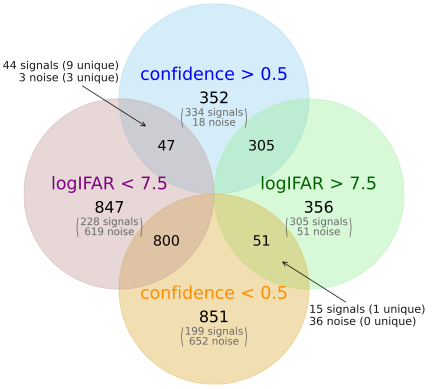
To further assess classifier consistency, we construct summary diagrams representing the different regions in the $\log_{10}$(IFAR) versus conditional confidence plots in Table II. The diagrams indicate the number of events in each region, and highlight how many events are correctly and incorrectly up and down-ranked.

We note that the few noise events which are incorrectly up-ranked by one of the classifiers are unique to that classifier. Meanwhile, there is broad agreement on the majority of up-ranked signals.

The classifiers all correctly down-rank some noise events where $\log_{10}$(IFAR) is above threshold, but also incorrectly down-rank a similar number of signals. XGBoost down-ranks significantly more signals than the other classifiers while MLP down-ranks the fewest signals.

Together, these results demonstrate that our framework remains robust to the choice of training dataset, with broadly consistent conditional confidence scores regardless of whether the MDC or LLPIC data are used for training and calibration. When the exchangeability assumption is deliberately broken (using MDC for training and LLPIC for testing), the ML classifiers continue to outperform maximum-$\log_{10}$IFAR in noise rejection, though XGBoost's down-rankings become less reliable

TABLE II. Comparison of the three ML classifiers trained and calibrated on MDC and tested on LLPIC. The total number of signals and noise in regions where the conditional confidence and $\log_{10}$(IFAR) disagree are annotated. We also note how many of these events are up or down-ranked by that classifier only.

LR	XGBoost	MLP
		

under this distribution shift. Importantly, XGBoost's up-rankings remain reliable under this distribution shift, correctly recovering BNS-like candidates analogous to GW200311_103121, and it retains the fewest false positives of all classifiers. Its down-rankings warrant some caution, but given its superior AUC and correct up-rankings, we continue to use XGBoost as our preferred classifier in the following analysis.

III. OBSERVATIONAL RESULTS

A. GWTC-4.1

We now apply our method for the first time to the O4a candidates in the updated GWTC-4.1 [1, 40] catalogue, and investigate the resulting classifications. GWTC-4.1 is an updated version of the O4a catalogue [40], incorporating a reanalysis of candidates by `PyCBC` and `GstLAL` with updated pipeline configurations [1].

We note that only the two LIGO detectors were operating during O4a [40]. As the larger mock dataset, we use the MDC as training and calibration data and restrict the features to the IFAR, SNR, and chirp mass as discussed in Section II. Similarly to O3, we find broad agreement between the conditional confidence and maximum-$p_{\rm astro}$, see Fig. 7 for the XGBoost classifier.

In the bottom-right quadrant of Fig. 7, we find candidates with $p_{\rm astro} \geq 0.5$ but conditional confidence below 0.5. The majority are low-significance triggers (FAR $\geq$ 1 per year) identified by only one or two pipelines. There are also eight high-significance events found in this quadrant. One example is GW230630_070659, a `GstLAL` offline-only candidate that was later found to have evidence of instrumental origin [40]. Follow-up data quality investigations [70] found excess power consistent with scattered light in both detectors at the time of the event,

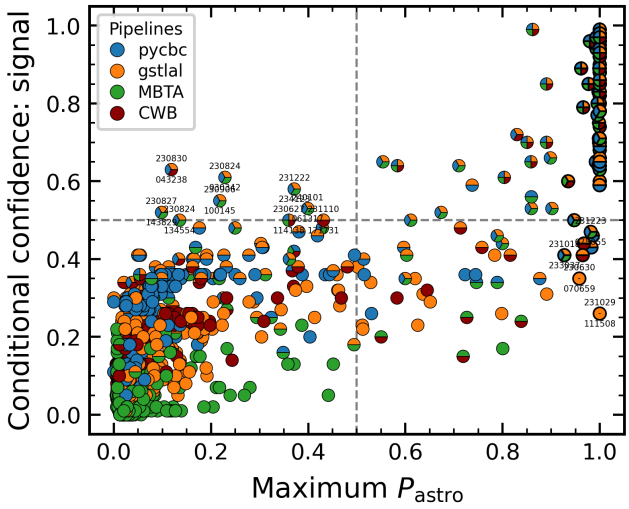


FIG. 7. The conditional confidence in the signal label for the XGBoost classifier compared to the maximum $p_{\rm astro}$ for the O4a events in the GWTC-4.1 catalogue. The classifier is trained and CP calibrated on the MDC data. The dashed lines represent the conditional confidence and $p_{\rm astro}$ thresholds, respectively. High-significance events (FAR $<$ 1 per year) are indicated by a bold marker outline. We highlight names of candidates discussed in the text.

rendering it inconsistent with a CBC signal, and no parameter estimation was performed for the catalogue [40]. Independent analyses by Emma et al. [71] find the data consistent with a BBH waveform but cannot provide evidence for an astrophysical origin, while Ashton et al. [72] conclude that a coincident pair of glitches is the likely explanation. Another example is GW231029_111508, a single-detector high-mass event found by `GstLAL` only. Its high detector-frame chirp mass and short duration place

it outside the parameter space for single-detector triggers of MBTA and PyCBC, respectively [40, 73].

The remaining high-significance candidates are low-to-moderate SNR events; GW230706_104333 and GW230729_082317 are low-mass events recovered by PyCBC and GstLAL, while GW231223_075055 is similarly low-mass but recovered by three pipelines, with high significance from PyCBC only. GW231004_232346 and GW231230_170116 are intermediate-mass two-pipeline events recovered with high significance in cWB only. GW231018_233037 is a three-pipeline candidate, recovered with high significance in MBTA only and required glitch mitigation in both detectors [40]. In all cases, the limited pipeline consensus may contribute to their classification as noise by the ML combination framework, as correlated high-significance recovery across pipelines is more characteristic of confident signals in the training population. A full list of all candidates in this quadrant, their $p_{\rm astro}$ and conditional confidence values, is presented in Table IX.

In the top-left quadrant of Fig. 7, we identify several BBH candidates that fall below the $p_{\rm astro}$ threshold but with conditional confidence values above threshold; the full list is given in Table VI. The majority are three-pipeline events recovered by GstLAL, MBTA, and PyCBC, with low SNR values in the range 7–8 and low significance across all pipelines. GW230627_114138 is additionally recovered by cWB, while GW231110_171731 is found by cWB and GstLAL only. Their correlated recovery across multiple pipelines is consistent with the pattern of genuine signals in the training data, resulting in above-threshold conditional confidence.

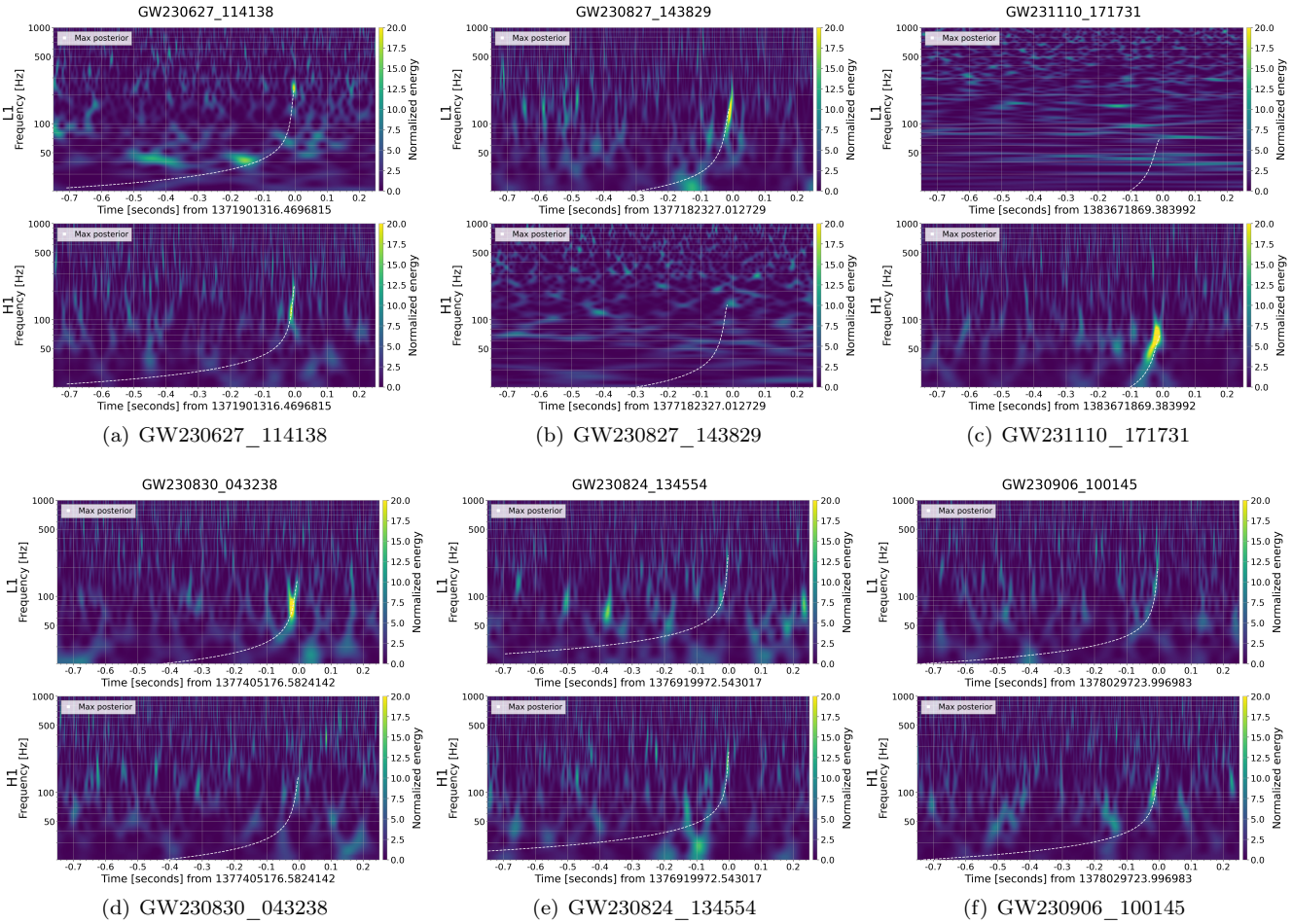
To further investigate these candidates, we also examine their time-frequency spectrograms in Fig. 8. To aid the interpretation, we also overlay the time-frequency evolution of the inspiral computed from the maximum-likelihood parameters of the Bayesian parameter estimation. We note that this only represents the peak of the posterior and carries uncertainty, particularly in the absolute merger time. At these low SNR values, even genuine CBC signals would produce only weak or indistinct excess power, so it is unsurprising that most spectrograms show no signal-like features. Nevertheless, several candidates exhibit some evidence of excess power in the LIGO detectors. GW230627_114138, Fig. 8(a), shows coincident excess power in both detectors, possibly resembling a chirp in H1, though L1 data quality issues complicate the interpretation. GW230827_143829, Fig. 8(b), and GW231110_171731, Fig. 8(c), each show a chirp-like feature in L1 and H1, respectively, while GW230830_043238, Fig. 8(d), shows transient power in L1 around the trigger time, resembling a chirp-like feature overlapping transient noise. GW230824_134554 and GW230906_100145 show faint, possibly chirp-like, coincident excess power in both detectors, see Figs. 8(e) and 8(f). The remaining candidates up-ranked by the XGBoost classifier show no discernible coincidence excess power. All additional time-frequency spectrograms can be found in the accompanying data release [74].

Next, we estimate their source parameters using the Bayesian inference code Bilby [75]. Following the same approach as in GWTC-5.0 [1], we use the IMRPhenomXPHM [76, 77] waveform model with the DYNESTY nested sampling package [78]. While parameter estimation cannot be used to determine whether a candidate is a real signal, it can provide further support for whether the properties of a candidate appear consistent with a CBC signal.

In Fig. 9, we show the resulting posteriors for a selection of parameters: source-frame chirp mass $\mathcal{M}$, mass ratio q, the source-frame component masses m_1 and m_2, effective inspiral spin $\chi_{\rm eff}$, effective precession spin $\chi_{\rm p}$, source inclination angle θ_{JN}, and luminosity distance D_L (see Table 3 in Abac et al. [79] for definitions). All of the events return source parameters consistent with stellar-mass BBH signals, with GW231110_171731 having the highest inferred component masses in the set. The majority of events are consistent with negligible aligned spins ($\chi_{\rm eff} \approx 0$); however, several events, GW230627_114138, GW230827_143829, GW230906_100145, and GW240101_061317 show support for positive $\chi_{\rm eff}$, suggestive of preferentially aligned spins. The mass ratios are broadly consistent with approximately equal mass binaries for most candidates; however, GW231222_234123 shows stronger support for unequal masses. The luminosity distances span $\sim$ 2–10 Gpc, placing some of these among the most distant BBH candidates observed. For comparison, the most distant confirmed GW event detected to date is GW190403_051519 at $d_L = 8.28^{+6.72}_{-4.29}$ Gpc [56], while the most distant candidate here is GW231110_171731 at $d_L = 9.50^{+5.81}_{-5.54}$ Gpc. Assuming these are actual astrophysical signals, the low significance of these events could at least partly be explained as a consequence of their large distances. A table summarising the median and 90% credible intervals for events and parameters shown in Fig. 9 is included in Appendix D in Table XI.

Furthermore, we can investigate the features of each event using SHAP values, and find that all candidates appear signal-like, following the method and discussion in Appendix B 4. The waterfall plots for all events are included in the data release [74].

Another candidate of interest from the fourth observing run is GW231109_235456, a sub-threshold GstLAL-only BNS which was later found with high significance by the GstLAL sub-threshold search [80]. In our analysis, based on the original pipeline outputs (SNR 9.64, $\log_{10}$(IFAR) 4.97, chirp mass 1.3), the candidate obtains conditional confidence below threshold for all of our classifiers. The reanalysis finds a FAR of 1 per 50 years (which corresponds to a $\log_{10}$(IFAR) of 9.2), SNR of 9.7, and detector frame chirp mass of 1.3 [80]. Using these new features, we obtain increased conditional confidence scores still below threshold for the LR (from 0.06 to 0.23) and XGBoost (from 0.28 to 0.36) classifiers. For MLP, the confidence increases from 0.3 to 0.61, bringing the event comfortably



(a) GW230627_114138 (b) GW230827_143829 (c) GW231110_171731

(d) GW230830_043238 (e) GW230824_134554 (f) GW230906_100145

FIG. 8. Time-frequency spectrograms for some of the up-ranked O4a subthreshold candidates in GWTC-4.1. The dashed white lines show the time-frequency evolution of the inspiral computed from the maximum likelihood parameters of the Bayesian parameter estimation.

above the threshold. However, as our training data does not include any events from the `GstLAL` sub-threshold search, this reanalysis violates exchangeability and is purely an illustrative observation.

In summary, the ML framework down-ranks candidates that lack correlated multi-pipeline support, including single-pipeline detections and events with known data quality issues, even where individual pipeline significance is high. Conversely, it up-ranks low-SNR events recovered coherently by multiple pipelines, where no single pipeline reports high significance individually. SHAP analysis confirms that for these up-ranked candidates the classification is dominated by the degree of correlated multi-pipeline recovery, the characteristic most strongly associated with signals in the training data. For the up-ranked candidates, their estimated source parameters are broadly consistent with BBH mergers observed by the LVK at large luminosity distances, lending further plausibility to an astrophysical origin.

B. GWTC-5.0

Next, we apply our method to the O4b candidates in the GWTC-5.0 [1] catalogue, and investigate the resulting classifications. We continue using the MDC as training and calibration data and restricting the features to the IFAR, SNR, and chirp mass of each pipeline.

Similarly to the previous analyses, we find broad agreement between the conditional confidence and maximum-$p_{\rm astro}$, but a few events where the two methods disagree, see Fig. 10 for the XGBoost classifier.

In the bottom-right quadrant of Fig. 10, we find candidates above the $p_{\rm astro}$ threshold but with conditional confidence below 0.5. A full list of all candidates in this quadrant, their $p_{\rm astro}$ and conditional confidence values, is presented in Table X. The majority are low-significance triggers identified by only one or two pipelines.

We also find six high-significance BBH candidates in this quadrant. GW240526_093944 and GW241230_084504 are single-pipeline candidates found only by `MBTA` and `GstLAL`, respectively.

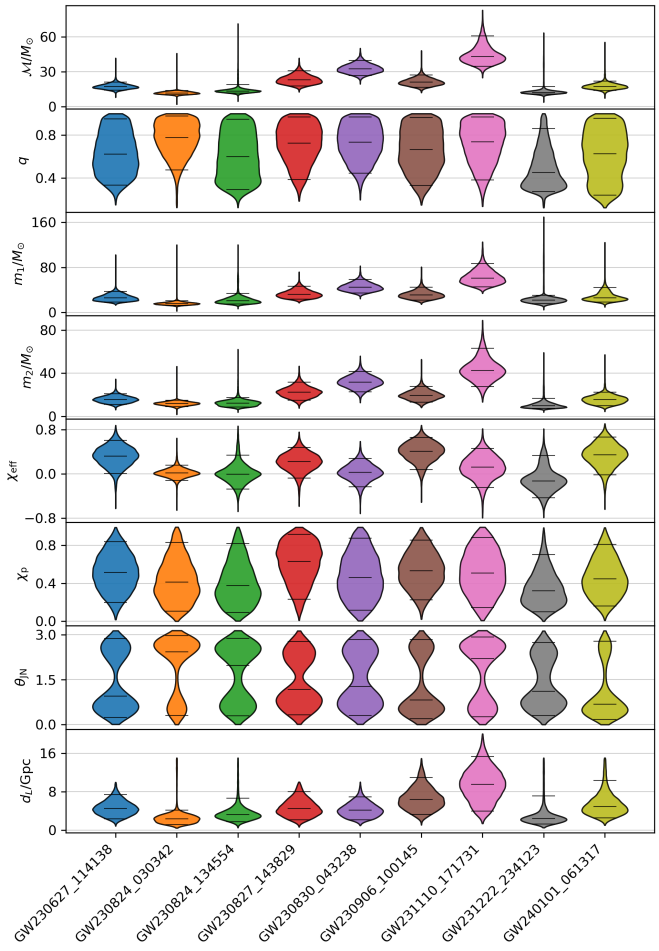


FIG. 9. Violin plots of estimated posterior distributions for O4a events in GWTC-4.1 with subthreshold $p_{\rm astro}$ but conditional confidence above threshold for XGBoost. The parameters shows are the source-frame chirp mass $\mathcal{M}$, mass ratio q, the source-frame component masses m_1 and m_2, effective inspiral spin $\chi_{\rm eff}$, effective precession spin $\chi_{\rm p}$, source inclination angle θ_{JN}, and luminosity distance D_L. Each violin displays the posterior distribution, with the median and the 90% interval indicated.

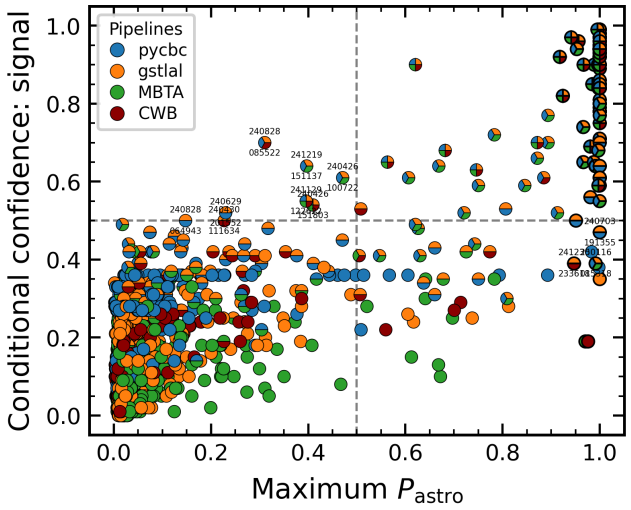


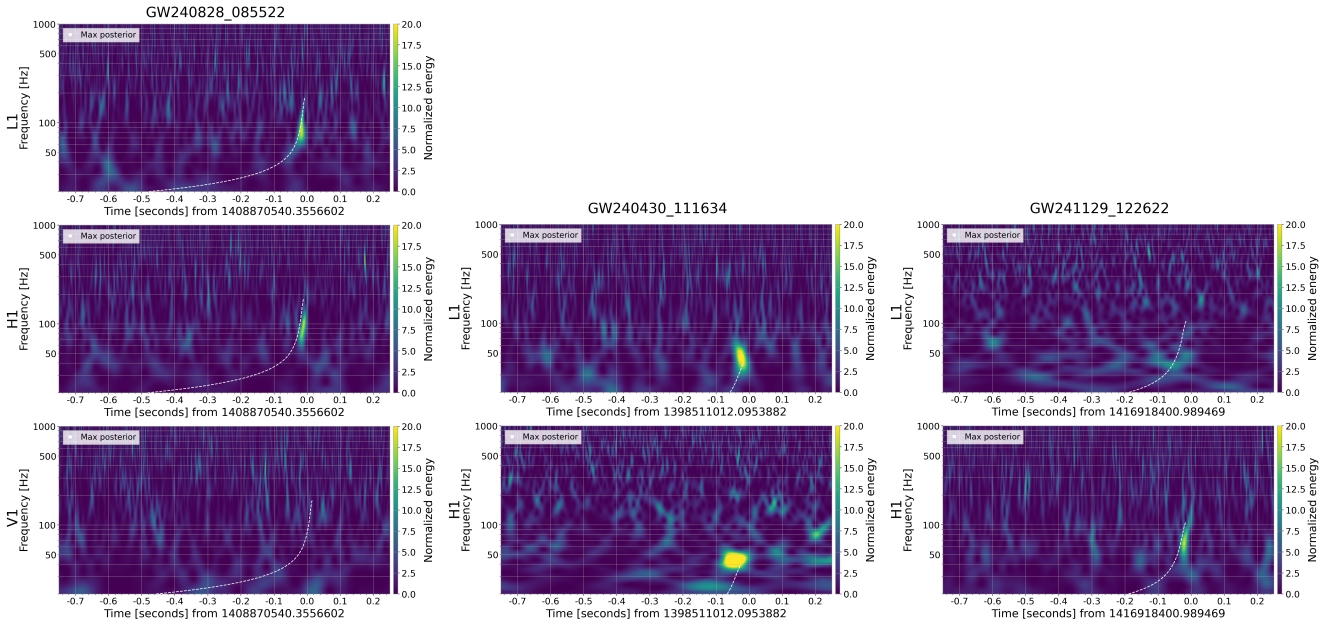
FIG. 10. The conditional confidence in the signal label for the XGBoost classifier compared to the maximum $p_{\rm astro}$ for the O4b events in the GWTC-5.0 catalogue. The classifier is trained and CP calibrated on the MDC data. The dashed lines represent the conditional confidence and $p_{\rm astro}$ thresholds, respectively. High-significance events (FAR $<$ 1 per year) are indicated by a bold marker outline. We highlight names of candidates discussed in the text.

GW240930_234614 is recovered exclusively by `cWB`, which may reduce confidence in the BBH nature of the candidate, though `cWB` could potentially identify signals affected by physical effects neglected by matched-filter searches, such as precession and eccentricity [1]. Additionally, parameter estimation reveals pronounced model-dependent differences across waveform approximants for this event [1]. GW240703_191355 and GW241230_233618 are two-pipeline events. GW240703_191355 is detected in the Livingston and Virgo detectors only, while GW241230_233618 has the highest total mass of any O4b candidate in the catalogue ($M \approx 116\,M_\odot$) as well as support for negative effective inspiral spin ($\chi_{\rm eff} \approx -0.14$) [1]. GW250116_015318 is a three-pipeline event, but the pipeline significances are highly discrepant and only `PyCBC` recovers it with high significance and above the $p_{\rm astro}$ threshold; notably only XGBoost down-ranks this candidate, while the other ML classifiers assign above threshold conditional confidence. In all cases, the limited or inconsistent pipeline consensus results in below-threshold confidence from the ML framework.

In the top-left quadrant of Fig. 10, we identify several BBH candidates that fall below the $p_{\rm astro}$ threshold but with conditional confidence values above threshold. The full list is given in Table VII. The majority of these are three- or four-pipeline candidates with low SNR. We also note that four of the eight up-ranked candidates occur in pairs on the same day: GW240426_100722 and GW240426_151803 are separated by approximately five hours, while GW240828_064943 and GW240828_085522 are separated by approximately two hours. The close temporal separations are notable, and if either pair is confirmed as astrophysical, the origin of the coincidence would warrant further investigation.

Investigating the time-frequency spectrograms, we observe a chirp-like feature coincident in both LIGO detectors for GW240828_085522, see Fig. 11(a). GW240430_111634, Fig. 11(b), shows coincident excess power in both LIGO detectors before the merger time. GW241129_122622, Fig. 11(c) shows excess power around the time of merger in H1.

The other up-ranked events show no signal-like features, but this is not unexpected as they are all low SNR (7–8) candidates and even genuine CBC signals would produce



(a) GW240828_085522 (b) GW240430_111634 (c) GW241129_122622

FIG. 11. Time-frequency spectrograms for some of the up-ranked O4b subthreshold candidates in GWTC-5.0. The dashed white lines show the time-frequency evolution of the inspiral computed from the maximum likelihood parameters of the Bayesian parameter estimation.

only weak or indistinct excess power at these SNR values.

Similarly to the previous section, we estimate the source parameters for all candidates up-ranked by the XGBoost classifier, as shown in Fig. 12. All candidates return posteriors consistent with BBH signals, with mass ratios broadly consistent with near-equal mass binaries. Chirp masses are mostly in the stellar-mass range, with the exception of GW240430_111634 ($\mathcal{M} \approx 80\,M_\odot$), which lies in the high-mass regime. With a total mass of $M = 190.15^{+52.67}_{-42.57}\,M_\odot$[1], GW240430_111634 would, if confirmed astrophysical, be one of the most massive BBH candidates detected to date (though not as massive as GW231123_135430, with $M = 236^{+29}_{-48}\,M_\odot$ [40, 81]). Notably, the primary component mass of GW240430_111634 ($m_1 \approx 109\,M_\odot$) falls in the intermediate-mass black hole regime.

Effective inspiral spins are broadly consistent with zero for all candidates, though GW240828_064943 and GW241219_151137 show mild support for positive $\chi_{\rm eff}$, suggestive of preferentially aligned spins. Luminosity distances span 4–11 Gpc, suggesting that, if of astrophysical origin, some of these would be among the most distant BBH candidates observed, with the most distant being GW241129_122622 at $d_L = 11.36^{+8.83}_{-5.99}$ Gpc, followed by GW240426_100722 at $d_L = 11.26^{+8.61}_{-5.54}$ Gpc. Both of these exceed the most distant up-ranked O4a candidate GW231110_171731 at $d_L = 9.50^{+5.81}_{-5.54}$ Gpc. The median parameter values and 90% credible intervals are tabulated in Table XII.

Lastly, we investigate the features of each event using SHAP values, and find that all up-ranked candidates appear signal-like, following the method and discussion in Appendix B 4. The plots are included in the data release [74].

As in the O4a analysis, the up-ranked candidates in O4b share a common profile of low-SNR events recovered coherently by multiple pipelines, with source parameters consistent with BBH mergers at large luminosity distances. Their correlated multi-pipeline recovery is the pattern most strongly associated with genuine signals in the training data, and provides the basis for the above-threshold conditional confidence assigned by the ML framework.

IV. DISCUSSION AND CONCLUSION

In this work, we have presented a systematic evaluation of our framework [44] for combining the outputs of multiple GW search pipelines using supervised ML together with CP. Rather than relying on simple combination rules such as the maximum IFAR or $p_{\rm astro}$, our approach learns an optimal mapping from multi-pipeline information to a calibrated confidence measure, trained on data where the ground truth is known. This enables the model to exploit correlations between pipelines and to adapt naturally to parameter-space-dependent sensitivities.

Applying our framework to real data from O3 and O4, we find several events with subthreshold $p_{\rm astro}$ values but

[1] This value had been corrected from a previous version.

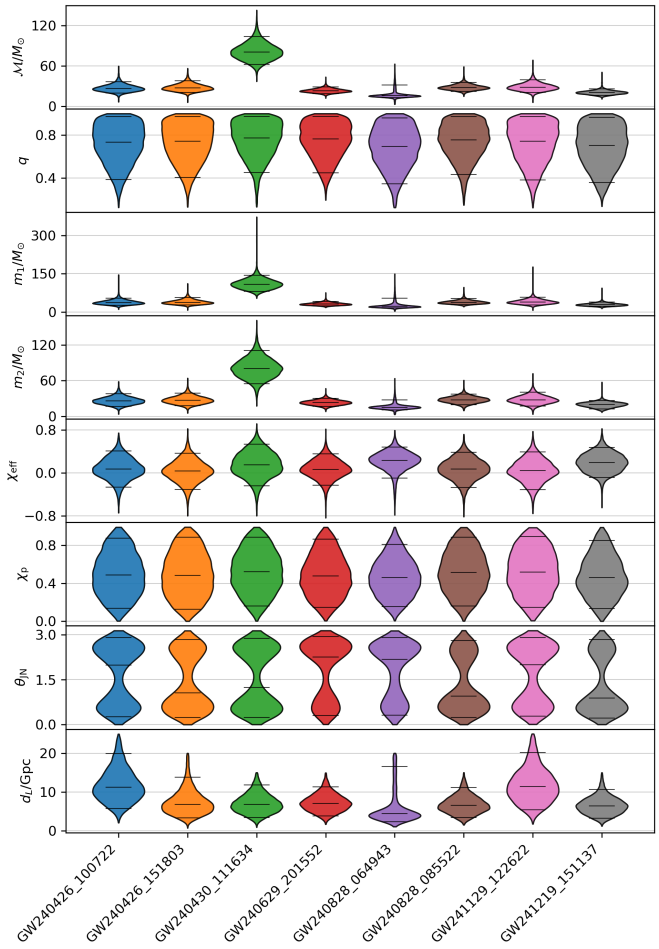


FIG. 12. Violin plots of estimated posterior distributions for O4b events in GWTC-5.0 with subthreshold $p_{\rm astro}$ but conditional confidence above threshold for XGBoost. The parameters shows are the source-frame chirp mass $\mathcal{M}$, mass ratio q, the source-frame component masses m_1 and m_2, effective inspiral spin $\chi_{\rm eff}$, effective precession spin $\chi_{\rm p}$, source inclination angle θ_{JN}, and luminosity distance D_L. Each violin displays the posterior distribution, with the median and the 90% interval indicated.

CP conditional confidence above threshold, most notably the marginal BNS candidate GW200311_103121. If real, it is only the third BNS signal detected. If our framework were applied in real time, an up-ranking of a subthreshold candidate such as this could lead to electromagnetic follow-up and the possibility of a multi-messenger detection, enabling the rich multi-messenger science that would follow. We also consistently up-rank the two marginal NSBH candidates GW190426_152155 and GW190531_023648 from GWTC-2.1, whose low $p_{\rm astro}$ values reflect prior uncertainty on the NSBH merger rate rather than weak pipeline significance.

When applied to O4a and O4b candidates, our framework identifies several subthreshold BBH candidates with elevated confidence. The up-ranked candidates share a common profile: low-SNR events in the range 7–8, recovered coherently by multiple pipelines, with no single pipeline reporting high individual significance. If of astrophysical origin, their source parameters are consistent with BBH mergers spanning stellar to intermediate masses, at luminosity distances of $\sim$ 2–11 Gpc, which would place some among the most distant GW events observed to date. Notably, the O4b candidate GW240430_111634 has an estimated total mass of $\sim 190\,M_\odot$, which would be among the most massive BBH candidates detected to date [40, 81]. Several candidates also show chirp-like features in their time-frequency spectrograms, lending further support to a potential astrophysical origin. Their sub-threshold individual significance is plausibly explained by their large distances, and their correlated multi-pipeline recovery is what distinguishes them from noise in the eyes of the classifier.

We validated the reliability of these results through a series of robustness checks. The framework produces broadly consistent results across different ML classifier architectures, indicating that the findings are driven by the multi-pipeline information rather than model-specific choices. CP is classifier-agnostic, so the framework is readily compatible with new classifiers as they become available. Results are also largely consistent when training and calibrating on two different mock datasets, the MDC and the smaller LLPIC, despite differences in dataset size and observing run configuration. A SHAP analysis confirms that the classifiers learn physically meaningful patterns, with detection significance features dominating and results consistent between the mock and real datasets. Based on its superior false positive control under distribution shift, we identify XGBoost as our preferred classifier.

A key consideration is whether the up-ranked events can be trusted. The validity of CP rests on the exchangeability of the calibration and test data, which cannot be guaranteed when training on mock data and testing on real events. We also note that the MDC has known limitations as a proxy for real data: the injected event rate is far higher than astrophysically expected, the pipelines were still under development, and the minimum IFAR threshold restricts the available noise statistics. A more realistic MDC with lower IFAR thresholds would strengthen the exchangeability assumption and improve confidence in the results. Nevertheless, while exchangeability cannot be guaranteed, we have empirically assessed the reliability of the framework through a series of consistency checks.

First, when training and calibrating on the MDC and evaluating on the LLPIC, mimicking the distribution shift between mock and real data, all ML classifiers achieve substantially lower false positive rates than maximum-$\log_{10}$IFAR, with XGBoost performing best. Moreover, most noise events misclassified by maximum-$\log_{10}$IFAR obtain sub-threshold confidence from all ML classifiers, suggesting the framework is conservative where it matters most.

Second, SHAP analysis of the up-ranked events confirms they exhibit signal-like characteristics, and parame-

ter estimation returns source parameters consistent with compact binary mergers, lending further support to their astrophysical interpretation.

Taken together, these consistency checks provide evidence that the up-ranked events correspond to genuine signal-like candidates, supporting their astrophysical interpretation, including that of GW200311_103121 as a BNS signal.

The framework also assigns sub-threshold conditional confidence to some candidates above the $p_{\rm astro}$ threshold, an effect that is most pronounced for XGBoost, which prioritises a low false positive rate over sensitivity. This reflects what the framework has learned from the training data: lack of agreement between pipelines is strongly associated with noise, so candidates without corroborated multi-pipeline recovery receive lower confidence, even when one pipeline reports high significance. Where individual pipelines have missed a real signal for legitimate reasons, such as gaps in template bank coverage or the absence of coincident triggers, genuine signals may thus be incorrectly down-ranked, as the apparent lack of pipeline agreement does not reflect their astrophysical nature. Conversely, in some cases the lower confidence correctly identifies noise, as illustrated by GW230630_070659, a high-significance single-pipeline candidate subsequently identified as having an instrumental origin [40].

More broadly, this framework is not intended to replace detailed pipeline-specific expertise, but to complement it by distilling diverse information into a unified measure that is readily usable by downstream analyses and astronomers responding to GW alerts. The approach is flexible: it can incorporate additional input features such as astrophysical probabilities or detector-state information, extends naturally to multi-class classification and real-time applications, and is readily extensible to additional pipelines provided mock data is available.

We therefore view this work as a step towards a more systematic and interpretable combination of GW search pipelines. By combining ML models with CP, this framework offers a robust path to producing catalogues and alerts with well-calibrated uncertainty estimates, supporting both confident detections and careful interpretation near threshold.

ACKNOWLEDGMENTS

We want to thank Thomas Sainrat for valuable suggestions and feedback, Tom Dent and Achal Kumar for their helpful discussions and assistance in diagnosing the confusion regarding the `cWB` pipeline outputs, and Sebastian Khan for discussions and feedback on the ML architecture and feature-importance methodology. We also thank Michael Coughlin, Deep Chatterjee, Tito Dal Canton, Reed Essick, Shaon Ghosh, Sushant Sharma-Chaudhary, Max Trevor, and Andrew Toivonen for the development of the MDC results used in this work. We use data from Chaudhary et al. [64] and thank the authors for preparing this dataset, and Sushant Sharma-Chaudhary and Thomas Sainrat for their help and advice in utilising it. Implementation of our ML models was done using `scikit-learn` [82] and `XGBoost` [66], while we utilise `NumPy` [83], `Pandas` [84], and `Matplotlib` [85] for data handling and visualisation. This material is based upon work supported by NSF's LIGO Laboratory, which is a major facility fully funded by the National Science Foundation. The authors are grateful for computational resources provided by the LIGO Laboratory and supported by National Science Foundation Grants PHY-0757058 and PHY-0823459. This work is supported by the Science and Technology Facilities Council (STFC) grant UKRI2488.

[1] A. G. Abac et al. GWTC-5.0: Observations from the Second Part of the Fourth LIGO-Virgo-KAGRA Observing Run and Updates to the Gravitational-Wave Transient Catalog. 5 2026.

[2] J. Aasi et al. Advanced LIGO. *Class. Quant. Grav.*, 32: 074001, 2015. doi:10.1088/0264-9381/32/7/074001.

[3] F. Acernese et al. Advanced Virgo: a second-generation interferometric gravitational wave detector. *Class. Quant. Grav.*, 32(2):024001, 2015. doi:10.1088/0264-9381/32/2/024001.

[4] T. Akutsu et al. Overview of KAGRA: Detector design and construction history. *PTEP*, 2021(5):05A101, 2021. doi:10.1093/ptep/ptaa125.

[5] B. P. Abbott et al. GW170817: Observation of Gravitational Waves from a Binary Neutron Star Inspiral. *Phys. Rev. Lett.*, 119(16):161101, 2017. doi:10.1103/PhysRevLett.119.161101.

[6] B. P. Abbott et al. A gravitational-wave standard siren measurement of the Hubble constant. *Nature*, 551(7678): 85–88, 2017. doi:10.1038/nature24471.

[7] B. P. Abbott et al. GW170817: Measurements of neutron star radii and equation of state. *Phys. Rev. Lett.*, 121 (16):161101, 2018. doi:10.1103/PhysRevLett.121.161101.

[8] Benjamin P Abbott et al. A guide to LIGO–Virgo detector noise and extraction of transient gravitational-wave signals. *Class. Quant. Grav.*, 37(5):055002, 2020. doi:10.1088/1361-6382/ab685e.

[9] A. G. Abac et al. GWTC-5.0: Methods for Identifying and Characterizing Gravitational-wave Transients. 5 2026.

[10] Will M. Farr, Jonathan R. Gair, Ilya Mandel, and Curt Cutler. Counting And Confusion: Bayesian Rate Estimation With Multiple Populations. *Phys. Rev. D*, 91(2): 023005, 2015. doi:10.1103/PhysRevD.91.023005.

[11] Cody Messick et al. Analysis Framework for the Prompt Discovery of Compact Binary Mergers in Gravitational-wave Data. *Phys. Rev. D*, 95(4):042001, 2017. doi:10.1103/PhysRevD.95.042001.

[12] Surabhi Sachdev et al. The GstLAL Search Analysis Methods for Compact Binary Mergers in Advanced LIGO's Second and Advanced Virgo's First Observing Runs. 1 2019.

[13] Leo Tsukada et al. Improved ranking statistics of the GstLAL inspiral search for compact binary coalescences. *Phys. Rev. D*, 108(4):043004, 2023. doi: 10.1103/PhysRevD.108.043004.

[14] Shio Sakon et al. Template bank for compact binary mergers in the fourth observing run of Advanced LIGO, Advanced Virgo, and KAGRA. *Phys. Rev. D*, 109(4): 044066, 2024. doi:10.1103/PhysRevD.109.044066.

[15] Prathamesh Joshi et al. New Methods for Offline GstLAL Analyses. 6 2025.

[16] Kipp Cannon et al. GstLAL: A software framework for gravitational wave discovery. 10 2020.

[17] Chad Hanna et al. Fast evaluation of multidetector consistency for real-time gravitational wave searches. *Phys. Rev. D*, 101(2):022003, 2020. doi: 10.1103/PhysRevD.101.022003.

[18] Christopher Alléné et al. The MBTA pipeline for detecting compact binary coalescences in the fourth LIGO-Virgo-KAGRA observing run. *Class. Quant. Grav.*, 42 (10):105009, 2025. doi:10.1088/1361-6382/add234.

[19] F. Aubin et al. The MBTA pipeline for detecting compact binary coalescences in the third LIGO–Virgo observing run. *Class. Quant. Grav.*, 38(9):095004, 2021. doi:10.1088/1361-6382/abe913.

[20] T. Adams, D. Buskulic, V. Germain, G. M. Guidi, F. Marion, M. Montani, B. Mours, F. Piergiovanni, and G. Wang. Low-latency analysis pipeline for compact binary coalescences in the advanced gravitational wave detector era. *Class. Quant. Grav.*, 33(17):175012, 2016. doi:10.1088/0264-9381/33/17/175012.

[21] Bruce Allen, Warren G. Anderson, Patrick R. Brady, Duncan A. Brown, and Jolien D. E. Creighton. FINDCHIRP: An Algorithm for detection of gravitational waves from inspiraling compact binaries. *Phys. Rev. D*, 85:122006, 2012. doi:10.1103/PhysRevD.85.122006.

[22] Tito Dal Canton et al. Implementing a search for aligned-spin neutron star-black hole systems with advanced ground based gravitational wave detectors. *Phys. Rev. D*, 90(8):082004, 2014. doi:10.1103/PhysRevD.90.082004.

[23] Samantha A. Usman et al. The PyCBC search for gravitational waves from compact binary coalescence. *Class. Quant. Grav.*, 33(21):215004, 2016. doi:10.1088/0264-9381/33/21/215004.

[24] Alexander H. Nitz, Thomas Dent, Tito Dal Canton, Stephen Fairhurst, and Duncan A. Brown. Detecting binary compact-object mergers with gravitational waves: Understanding and Improving the sensitivity of the PyCBC search. *Astrophys. J.*, 849(2):118, 2017. doi:10.3847/1538-4357/aa8f50.

[25] Bruce Allen. χ^2 time-frequency discriminator for gravitational wave detection. *Phys. Rev. D*, 71:062001, 2005. doi:10.1103/PhysRevD.71.062001.

[26] Gareth S. Davies, Thomas Dent, Márton Tápai, Ian Harry, Connor McIsaac, and Alexander H. Nitz. Extending the PyCBC search for gravitational waves from compact binary mergers to a global network. *Phys. Rev. D*, 102(2):022004, 2020. doi:10.1103/PhysRevD.102.022004.

[27] Qi Chu et al. SPIIR online coherent pipeline to search for gravitational waves from compact binary coalescences. *Phys. Rev. D*, 105(2):024023, 2022. doi: 10.1103/PhysRevD.105.024023.

[28] Jing Luan, Shaun Hooper, Linqing Wen, and Yanbei Chen. Towards low-latency real-time detection of gravitational waves from compact binary coalescences in the era of advanced detectors. *Phys. Rev. D*, 85:102002, 2012. doi:10.1103/PhysRevD.85.102002.

[29] Tanmaya Mishra, Shubhagata Bhaumik, V. Gayathri, Marek J. Szczepańczyk, Imre Bartos, and Sergey Klimenko. Gravitational waves detected by a burst search in LIGO/Virgo's third observing run. *Phys. Rev. D*, 111 (2):023054, 2025. doi:10.1103/PhysRevD.111.023054.

[30] S. Klimenko, S. Mohanty, Malik Rakhmanov, and Guenakh Mitselmakher. Constraint likelihood analysis for a network of gravitational wave detectors. *Phys. Rev. D*, 72:122002, 2005. doi:10.1103/PhysRevD.72.122002.

[31] S. Klimenko, I. Yakushin, A. Mercer, and Guenakh Mitselmakher. Coherent method for detection of gravitational wave bursts. *Class. Quant. Grav.*, 25:114029, 2008. doi:10.1088/0264-9381/25/11/114029.

[32] S. Klimenko et al. Method for detection and reconstruction of gravitational wave transients with networks of advanced detectors. *Phys. Rev. D*, 93(4):042004, 2016. doi:10.1103/PhysRevD.93.042004.

[33] S. Klimenko and Guenakh Mitselmakher. A wavelet method for detection of gravitational wave bursts. *Class. Quant. Grav.*, 21:S1819–S1830, 2004. doi:10.1088/0264-9381/21/20/025.

[34] S. Klimenko, G. Vedovato, M. Drago, G. Mazzolo, G. Mitselmakher, C. Pankow, G. Prodi, V. Re, F. Salemi, and I. Yakushin. Localization of gravitational wave sources with networks of advanced detectors. *Phys. Rev. D*, 83:102001, 2011. doi:10.1103/PhysRevD.83.102001.

[35] Ethan Marx et al. Machine-learning pipeline for real-time detection of gravitational waves from compact binary coalescences. *Phys. Rev. D*, 111(4):042010, 2025. doi: 10.1103/PhysRevD.111.042010.

[36] Vasileios Skliris, Michael R. K. Norman, and Patrick J. Sutton. Toward real-time detection of unmodeled gravitational wave transients using convolutional neural networks. *Phys. Rev. D*, 110(10):104034, 2024. doi: 10.1103/PhysRevD.110.104034.

[37] Alexander H. Nitz, Sumit Kumar, Yi-Fan Wang, et al. 4-OGC: Catalog of Gravitational Waves from Compact Binary Mergers. *Astrophys. J.*, 946(2):59, 2023. doi: 10.3847/1538-4357/aca591.

[38] Ajit Kumar Mehta, Seth Olsen, Digvijay Wadekar, Javier Roulet, Tejaswi Venumadhav, Jonathan Mushkin, Barak Zackay, and Matias Zaldarriaga. New binary black hole mergers in the LIGO-Virgo O3b data. *Phys. Rev. D*, 111 (2):024049, 2025. doi:10.1103/PhysRevD.111.024049.

[39] R. Abbott et al. Gwtc-3: Compact binary coalescences observed by ligo and virgo during the second part of the third observing run. *Phys. Rev. X*, 13:041039, Dec 2023. doi:10.1103/PhysRevX.13.041039. URL `https://link.aps.org/doi/10.1103/PhysRevX.13.041039`.

[40] A. G. Abac et al. GWTC-4.0: Updating the Gravitational-Wave Transient Catalog with Observations from the First Part of the Fourth LIGO-Virgo-KAGRA Observing Run. 8 2025.

[41] Sharan Banagiri, Christopher P. L. Berry, Gareth S. Cabourn Davies, Leo Tsukada, and Zoheyr Doctor. Unified pastro for gravitational waves: Consistently combining information from multiple search pipelines. *Phys. Rev. D*, 108(8):083043, 2023. doi:

10.1103/PhysRevD.108.083043.

[42] Seiya Tsukamoto, Andrew Toivonen, Holton Griffin, Avyukt Raghuvanshi, Megan Averill, Frank Kerkow, Michael W. Coughlin, Man Leong Chan, and Leo Singer. Astrophysical or Terrestrial: Machine Learning Classification of Gravitational-wave Candidates Using Multiple-search Information. *Publ. Astron. Soc. Pac.*, 138(1): 014503, 2026. doi:10.1088/1538-3873/ae1e2e.

[43] Nikolas Moustakidis, Theofilo Moustakidis, Deep Chatterjee, Anastasios Tefas, and Erik Katsavounidis. The best of all worlds: gravitational-wave transient detection with multiple pipelines. 2026. in preparation.

[44] Gregory Ashton, Ann-Kristin Malz, and Nicolo Colombo. Enhancing Gravitational-Wave Detection: A Machine Learning Pipeline Combination Approach with Robust Uncertainty Quantification. *Phys. Rev. Lett.*, 136(1): 011402, 2026. doi:10.1103/yfb3-fgf2.

[45] Vladimir Vovk, Alexander Gammerman, and Glenn Shafer. *Algorithmic learning in a random world*, volume 29. Springer, 2005.

[46] Anastasios N Angelopoulos and Stephen Bates. A gentle introduction to conformal prediction and distribution-free uncertainty quantification. *arXiv preprint arXiv:2107.07511*, 2021.

[47] Gregory Ashton, Nicolo Colombo, Ian Harry, and Surabhi Sachdev. Calibrating gravitational-wave search algorithms with conformal prediction. *Phys. Rev. D*, 109 (12):123027, 2024. doi:10.1103/PhysRevD.109.123027.

[48] Evan Jones, Tuan Do, Yun Qi Li, Kevin Alfaro, Jack Singal, and Bernie Boscoe. Redshift Prediction with Images for Cosmology Using a Bayesian Convolutional Neural Network with Conformal Predictions. *Astrophys. J.*, 974 (2):159, October 2024. doi:10.3847/1538-4357/ad6d5a.

[49] Jonathan Soriano, Tuan Do, Srinath Saikrishnan, Vikram Seenivasan, Bernie Boscoe, Jack Singal, and Evan Jones. Improving Generalization and Uncertainty Quantification of Photometric Redshift Models. *Astron. J.*, 171(2):114, 2026. doi:10.3847/1538-3881/ae2ffe.

[50] Raquel Pezoa, Luis Salinas, Claudio Torres, Felipe Ortiz, Michel Cure, and Ignacio Araya. Uncertainty Estimation in Classification of Massive Stars Spectra using Conformal Predictions. In *2024 43rd International Conference of the Chilean Computer Science Society (SCCC)*, page 43. IEEE, October 2024. doi: 10.1109/SCCC63879.2024.10767640.

[51] Suk Yee Yong and Cheng Soon Ong. Uncertainty quantification of the virial black hole mass with conformal prediction. *Mon. Not. Roy. Astron. Soc.*, 524(2):3116–3129, 2023. doi:10.1093/mnras/stad2080.

[52] Marlon M. S. Mendes, Roberta Duarte Pereira, Mariana Dutra da Rosa Louren, and César H. Lenzi. Certified Uncertainty for Surrogate Models of Neutron Star Equations of State via Mondrian Conformal Prediction. 2 2026.

[53] Naomi Singer, Jonathan P. Williams, and Sujit Ghosh. Conformal prediction for astronomy data with measurement error. *Monthly Notices Royal Astronomical Society*, 539(2):1372–1380, May 2025. doi: 10.1093/mnras/staf515.

[54] Jack Y. Araz and Michael Spannowsky. Another Fit Bites the Dust: Conformal Prediction as a Calibration Standard for Machine Learning in High-Energy Physics. 12 2025.

[55] Ann-Kristin Malz, Gregory Ashton, and Nicolo Colombo. Classification uncertainty for transient gravitational-wave noise artifacts with optimized conformal prediction. *Phys. Rev. D*, 111(8):084078, 2025. doi: 10.1103/PhysRevD.111.084078.

[56] R. Abbott et al. GWTC-2.1: Deep Extended Catalog of Compact Binary Coalescences Observed by LIGO and Virgo During the First Half of the Third Observing Run. 8 2021.

[57] B. P. Abbott et al. GW190425: Observation of a Compact Binary Coalescence with Total Mass $\sim 3.4 M_{\odot}$. *Astrophys. J. Lett.*, 892(1):L3, 2020. doi:10.3847/2041-8213/ab75f5.

[58] Glenn Shafer and Vladimir Vovk. A tutorial on conformal prediction. *Journal of Machine Learning Research*, 9: 371–421, 2008. doi:10.48550/arXiv.0706.3188.

[59] LIGO Scientific Collaboration and Virgo Collaboration. Gwtc-2.1: Deep extended catalog of compact binary coalescences observed by ligo and virgo during the first half of the third observing run - candidate data release, July 2021. URL `https://doi.org/10.5281/zenodo.5759108`.

[60] LIGO Scientific Collaboration, Virgo Collaboration, and KAGRA Collaboration. Gwtc-3: Compact binary coalescences observed by ligo and virgo during the second part of the third observing run — candidate data release, November 2021. URL `https://doi.org/10.5281/zenodo.5546665`.

[61] LIGO Scientific Collaboration, Virgo Collaboration, and KAGRA Collaboration. Gwtc-4.1: Candidate data release, May 2026. URL `https://doi.org/10.5281/zenodo.20276095`.

[62] LIGO Scientific Collaboration, Virgo Collaboration, and KAGRA Collaboration. Gwtc-5.0: Candidate data release, May 2026. URL `https://doi.org/10.5281/zenodo.20348004`.

[63] Sushant Sharma Chaudhary et al. Low-latency gravitational wave alert products and their performance at the time of the fourth LIGO-Virgo-KAGRA observing run. *Proc. Nat. Acad. Sci.*, 121(18):e2316474121, 2024. doi:10.1073/pnas.2316474121.

[64] Sushant Sharma Chaudhary et al. Low-latency gravitational wave alert infrastructure and new data products for multi-messenger astronomy during ligo-virgo-kagras fourth observing run. 2026. in preparation.

[65] David E Rumelhart, Geoffrey E Hinton, and Ronald J Williams. Learning representations by back-propagating errors. *nature*, 323(6088):533–536, 1986.

[66] Tianqi Chen and Carlos Guestrin. XGBoost: A Scalable Tree Boosting System. 3 2016. doi: 10.1145/2939672.2939785.

[67] Vladimir Vovk. Conditional validity of inductive conformal predictors. *Machine Learning*, 92, 2013.

[68] Scott M Lundberg and Su-In Lee. A unified approach to interpreting model predictions. In I. Guyon, U. Von Luxburg, S. Bengio, H. Wallach, R. Fergus, S. Vishwanathan, and R. Garnett, editors, *Advances in Neural Information Processing Systems*, volume 30. Curran Associates, Inc., 2017. URL `https://proceedings.neurips.cc/paper_files/paper/2017/file/8a20a8621978632d76c43dfd28b67767-Paper.pdf`.

[69] Trevor Hastie, Robert Tibshirani, Jerome Friedman, et al. The elements of statistical learning, 2009.

[70] S. Soni et al. LIGO Detector Characterization in the first half of the fourth Observing run. *Class. Quant. Grav.*,

42(8):085016, 2025. doi:10.1088/1361-6382/adc4b6.

[71] Mattia Emma, Ann-Kristin Malz, Adriana Dias, and Gregory Ashton. Case studies with GPBilby of glitch-contaminated transient gravitational waves. 4 2026.

[72] Gregory Ashton, Colm Talbot, Andrew Lundgren, Ann-Kristin Malz, and Joseph Areeda. Measuring the rate of glitches in interferometric gravitational wave detectors with a hierarchical Bayesian model. 4 2026.

[73] A. G. Abac et al. GWTC-4.0: Methods for Identifying and Characterizing Gravitational-wave Transients. 8 2025.

[74] Ann-Kristin Malz, Samuel Russell, Gregory Ashton, and nicolo colombo. Data release: Combining gravitational wave search pipelines to find subthreshold signals in gwtc-5.0, July 2026. URL `https://doi.org/10.5281/zenodo.21258511`.

[75] Gregory Ashton et al. BILBY: A user-friendly Bayesian inference library for gravitational-wave astronomy. *Astrophys. J. Suppl.*, 241(2):27, 2019. doi:10.3847/1538-4365/ab06fc.

[76] Geraint Pratten et al. Computationally efficient models for the dominant and subdominant harmonic modes of precessing binary black holes. *Phys. Rev. D*, 103(10): 104056, 2021. doi:10.1103/PhysRevD.103.104056.

[77] Marta Colleoni, Felip A. Ramis Vidal, Cecilio García-Quirós, Sarp Akçay, and Sayantani Bera. Fast frequency-domain gravitational waveforms for precessing binaries with a new twist. *Phys. Rev. D*, 111(10):104019, 2025. doi:10.1103/PhysRevD.111.104019.

[78] Joshua S. Speagle. dynesty: a dynamic nested sampling package for estimating Bayesian posteriors and evidences. *Mon. Not. Roy. Astron. Soc.*, 493(3):3132–3158, 2020. doi:10.1093/mnras/staa278.

[79] A. G. Abac et al. GWTC-4.0: An Introduction to Version 4.0 of the Gravitational-Wave Transient Catalog. *Astrophys. J. Lett.*, 995(1):L18, 2025. doi:10.3847/2041-8213/ae0c06.

[80] Wanting Niu et al. GW231109_235456: A Sub-threshold Binary Neutron Star Merger in the LIGO-Virgo-KAGRA O4a Observing Run? 9 2025.

[81] A. G. Abac et al. GW231123: A Binary Black Hole Merger with Total Mass 190–265 $M_\odot$. *Astrophys. J. Lett.*, 993(1):L25, 2025. doi:10.3847/2041-8213/ae0c9c.

[82] Lars Buitinck et al. API design for machine learning software: experiences from the scikit-learn project. 9 2013.

[83] Charles R Harris, K Jarrod Millman, Stéfan J van der Walt, Ralf Gommers, Pauli Virtanen, David Cournapeau, Eric Wieser, Julian Taylor, Sebastian Berg, Nathaniel J Smith, et al. Array programming with numpy. *Nature*, 585(7825):357–362, 2020.

[84] The pandas development team. pandas-dev/pandas: Pandas, February 2020. URL `https://doi.org/10.5281/zenodo.3509134`.

[85] John D. Hunter. Matplotlib: A 2d graphics environment. *Computing In Science & Engineering*, 9(3):90–95, May-Jun 2007.

[86] Vaibhav Tiwari, S. Klimenko, V. Necula, and G. Mitselmakher. Reconstruction of chirp mass in searches for gravitational wave transients. *Class. Quant. Grav.*, 33 (1):01LT01, 2016. doi:10.1088/0264-9381/33/1/01LT01.

[87] David R Cox. The regression analysis of binary sequences. *Journal of the Royal Statistical Society Series B: Statistical Methodology*, 20(2):215–232, 1958.

[88] Ciyou Zhu, Richard H. Byrd, Peihuang Lu, and Jorge Nocedal. Algorithm 778: L-BFGS-B. *ACM Trans. Math. Software*, 23(4):550–560, 1997. doi: 10.1145/279232.279236.

[89] Vinod Nair and Geoffrey E Hinton. Rectified linear units improve restricted boltzmann machines. In *Proceedings of the 27th international conference on machine learning (ICML-10)*, pages 807–814, 2010.

[90] Abien Fred Agarap. Deep Learning using Rectified Linear Units (ReLU). 3 2018.

[91] Diederik P. Kingma and Jimmy Ba. Adam: A Method for Stochastic Optimization. 12 2014.

[92] Thomas Cover and Peter Hart. Nearest neighbor pattern classification. *IEEE transactions on information theory*, 13(1):21–27, 1967.

[93] Tiffany Ding, Anastasios N. Angelopoulos, Stephen Bates, Michael I. Jordan, and Ryan J. Tibshirani. Class-conditional conformal prediction with many classes. *CoRR*, abs/2306.09335, 2023. doi: 10.48550/arXiv.2306.09335. URL `https://doi.org/10.48550/arXiv.2306.09335`.

[94] Gregory Ashton and Tim Dietrich. The use of hypermodels to understand binary neutron star collisions. *Nature Astron.*, 6(8):961–967, 2022. doi:10.1038/s41550-022-01707-x.

[95] R. Abbott et al. GWTC-2: Compact Binary Coalescences Observed by LIGO and Virgo During the First Half of the Third Observing Run. *Phys. Rev. X*, 11: 021053, 2021. doi:10.1103/PhysRevX.11.021053.

[96] Yin-Jie Li, Ming-Zhe Han, Shao-Peng Tang, Yuan-Zhu Wang, Yi-Ming Hu, Qiang Yuan, Yi-Zhong Fan, and Da-Ming Wei. GW190426_152155: a merger of neutron star-black hole or low mass binary black holes? 12 2020.

[97] Marlin B. Schäfer and Alexander H. Nitz. From one to many: A deep learning coincident gravitational-wave search. *Phys. Rev. D*, 105(4):043003, 2022. doi: 10.1103/PhysRevD.105.043003.

[98] Jesse Davis and Mark Goadrich. The relationship between precision-recall and roc curves. In *Proceedings of the 23rd international conference on Machine learning*, pages 233–240, 2006.

[99] Takaya Saito and Marc Rehmsmeier. The precision-recall plot is more informative than the roc plot when evaluating binary classifiers on imbalanced datasets. *PloS one*, 10(3):e0118432, 2015.

[100] Neil J Perkins and Enrique F Schisterman. The inconsistency of "optimal" cutpoints obtained using two criteria based on the receiver operating characteristic curve. *American journal of epidemiology*, 163(7):670–675, 2006.

[101] Scott M Lundberg, Gabriel Erion, Hugh Chen, Alex DeGrave, Jordan M Prutkin, Bala Nair, Ronit Katz, Jonathan Himmelfarb, Nisha Bansal, and Su-In Lee. From local explanations to global understanding with explainable ai for trees. *Nature machine intelligence*, 2 (1):56–67, 2020.

Appendix A: Method details

1. Data preparation

The pipeline outputs include both significance statistics and source parameter estimates. From the template-based pipelines, we use the reported FAR, SNR, and χ^2 (a matched-filter signal-consistency test [11, 25]). These pipelines also provide estimates of source parameters from the nearest waveform template. We record the detector-frame chirp mass, component masses, and aligned spin. As the `cWB` pipeline does not rely on an explicit waveform model, it does not provide template-based parameter estimates, and we thus only record the FAR and SNR. Although `cWB` internally derives a detector-frame chirp mass estimate from the time-frequency morphology of the reconstructed signal for use in its vetoes and classifier [9, 86], we do not include it here since this estimate relies on a different methodology than the template-based pipelines and may be subject to systematics that are not yet well understood; incorporating it is left for future work. We note that `cWB` records SNR^2 as the parameter named SNR, and correct for this when assembling our dataset. The SNR reported by `cWB` is a coherent, energy-based statistic [9] rather than a matched-filter SNR as used by the template-based pipelines, although both quantify the overall detection significance of a candidate. In all cases, we use the logarithm of the IFAR in units of seconds instead of the FAR, since variations in statistical significance are meaningful on a logarithmic rather than a linear scale. This choice also ensures that non-detections, for which no IFAR is reported, can be consistently assigned a value of zero. Both modelled and unmodelled searches produce additional diagnostic features which we do not include in the present analysis and whose utility would need to be assessed for a production-level implementation.

To train the ML classifier and calibrate CP, a labelled dataset that is exchangeable with the real data is required. In Ashton et al. [44] and for the majority of this work, we use the pre-O4 MDC study [63], which applied the `GstLAL`, `PyCBC`, `SPIIR`, `MBTA`, and `cWB` pipelines to 40 days of replayed data from the third observing run with injected signals. Secondly, we also consider the LLPIC dataset [64], produced during the maintenance break towards the end of the fourth observing (O4) run by injecting signals into replayed O4 background data. The LLPIC consisted of four one-week replay cycles; we use only the last 7 days, as this cycle is covered by the most pipelines. Candidates in both datasets with IFAR $>$ 1 hr are time-clustered, retaining only the maximum SNR candidate per pipeline.

This produces feature datasets containing per-pipeline detection statistics and template source parameter estimates, with feature values for non-detections set to zero. Ground-truth labels are assigned by matching candidates to known injections and astrophysical signals, yielding 9948 candidates, of which 5910 are signals for the MDC dataset and 1204 candidates, including 534 signals, for the LLPIC data. We note that the signal rate is far higher than astrophysically expected in both mock datasets. This inflated signal rate means that p_{astro} values and precision estimates computed from the mock data are not physically representative [63], and should be interpreted only as relative performance comparisons within the mock-data context. For this reason, we do not use p_{astro} as a comparison metric for the mock data studies, and instead compare against the maximum-$\log_{10}$IFAR method. For most experiments in this work, each dataset is split into training (80%), calibration (10%), and testing (10%) subsets. However, we also use the entire LLPIC dataset for testing only in Section II B 2.

In this work, we only use the `cWB`, `PyCBC`, `GstLAL`, and `MBTA` pipelines, as they have been applied to all datasets considered in this study. However, this framework can be applied to other pipelines as well, provided sufficient labelled training and calibration data exist. For mock data studies, we use all 21 features per pipeline, where available, as discussed in Ashton et al. [44]: the network $\log_{10}(\mathrm{IFAR})$ and SNR, and the template chirp mass, plus the per-detector SNR, χ^2, component masses, and aligned spins for each of the H1, L1, and V1 detectors. This establishes the classifier performance achievable when all pipeline information is available. When applying our method to the new candidates in GWTC-2.1 [56, 59], GWTC-3.0 [39, 60], GWTC-4.1 [40, 61], and GWTC-5.0 [1, 62], we restrict the features to the measured IFAR, SNR, and chirp mass (setting the chirp mass to zero for `cWB`). These are chosen to ensure better exchangeability across datasets: the IFAR and SNR are fundamental detection statistics that are consistently calibrated and validated across pipeline versions, while the chirp mass, though template-derived, is the most robustly measured source parameter and provides source classification information. This choice is further supported by the finding in Ashton et al. [44] that including additional features does not improve classification performance significantly, though further feature selection analysis could refine this choice.

However, differences in detector noise characteristics, pipeline configurations, and astrophysical signal rates between the mock data and the different catalogues may introduce systematic differences in the pipeline behaviour. Furthermore, in GWTC-3.0 the `PyCBC` pipeline performed a second, BBH-only search [39], which we exclude to ensure exchangeability.

2. Machine learning classifiers

In our previous work [44], we focused primarily on LR due to its interpretability. Here, we explore additional classifiers and compare the performance of LR, MLP, K-nearest neighbours (KNN), and XGBoost, a tree-based method. We implement the first three using `scikit-learn` [82], and use the `XGBoost` package [66] for the latter.

For each classifier, the ML model receives a feature vector $\vec{X}$ (the pipeline outputs for a candidate) and outputs

a probability $P_y(\vec{X};\lambda)$ for each label y, where λ denotes the model parameters.

The model parameters λ (weights and biases) are learned from the training data by minimising the cross-entropy loss, or equivalently maximising the log-likelihood. For a labelled training dataset of size N, the log-likelihood is written as

$$\sum_{n=1}^{N}\Big(Y_n\log(P_{y=1}(\vec{X}_n;\lambda))+(1-Y_n)\log(1-P_{y=1}(\vec{X}_n;\lambda))\Big)\,, \tag{A1}$$

where $Y_n\in\{0,1\}$ is the true label of the nth sample (one for signal, zero for noise), $\vec{X}_n$ is its feature vector, and $P_{y=1}(\vec{X}_n;\lambda)$ is the predicted probability for the signal label.

During training, the model parameters that maximise the log-likelihood in Eq. (A1), $\hat{\lambda}$, are estimated. The specific maximisation algorithm varies by classifier, as described below. After training, the learned model can evaluate previously unseen data, $\vec{X}'$ by computing $P_y(\vec{X}';\hat{\lambda})$.

a. *Logistic Regression (LR)*

LR [87] is a simple ML model, with $\lambda=(\vec{w},b)$, that maps a linear combination of input features to a probability through the sigmoid activation function $\sigma(z)$,

$$P_{y=1}(\vec{X};\lambda)=\sigma(z)=\frac{1}{1+\exp(-z)}\,, \tag{A2}$$

where

$$z=\vec{w}\cdot\vec{X}+b\,. \tag{A3}$$

The model is trained by maximising the log-likelihood in Eq. (A1) using the `L-BFGS-B` optimisation algorithm [88].

The magnitude of the LR coefficients w_i indicates the strength of feature i, while the sign indicates the direction of influence. LR is simple, interpretable, and computationally efficient, but its predictions are constrained by the linear relationship with the input features, which may limit flexibility on more complex datasets.

b. *Multi-layer Perceptron (MLP)*

MLP [65] is a feedforward artificial neural network in which the input feature vector $\vec{X}$ is sequentially transformed through layers of neurons to produce a probability for each class. In our implementation, the neural network consists of a single hidden layer of $K=100$ neurons (we find only minor improvements when investigating deeper models, but at the cost of decreased computational efficiency). Each neuron in the hidden layer computes a weighted sum of the input features plus a bias and applies the ReLU (rectified linear unit) activation function [89, 90] (which is defined as $\mathrm{ReLU}(x)=\max(0,x)$). The outputs of the hidden layer are then combined in the output layer using the sigmoid activation function to produce the final probability $P_{y=1}(\vec{X};\lambda)=\sigma(z)$, with

$$z=b^o+\sum_{k=1}^{K}w_k^o\,\mathrm{ReLU}\left(\vec{w}_k^h\cdot\vec{X}+b_k^h\right)\,. \tag{A4}$$

The weights and biases $\vec{w}^h$, b^h correspond to the K neurons in the hidden layer, while $\vec{w}^o$, b^o are associated with the output neuron.

Similarly to LR, the model parameters are optimised by maximising the log-likelihood in Eq. (A1), here using `Adam`, a stochastic gradient-based optimiser [91]. Unlike LR, MLPs can capture complex, non-linear relationships between features through their hidden layers, but require careful tuning and interpretation is less straightforward.

c. *k-Nearest Neighbours (KNN)*

KNN [92] is a non-parametric, instance-based model. For a given test feature vector $\vec{X}'$, the classifier identifies the k closest training points according to a chosen metric (we use the Minkowski distance with $p=2$, equivalent to Euclidean distance). The output probability $P_y(\vec{X}')$ is then calculated as the fraction of neighbours belonging to each class:

$$P_y(\vec{X}')=\frac{1}{k}\sum_{i\in\mathcal{N}_k(\vec{X}')}\mathbf{1}\{Y_i=y\}\,, \tag{A5}$$

where $\mathcal{N}_k(\vec{X}')$ denotes the indices of the k nearest neighbours of $\vec{X}'$ in the training set, Y_i is the true label of neighbour i, and $\mathbf{1}\{\cdot\}$ is the indicator function.

Unlike LR and MLP, KNN does not require explicit training and has no weights to optimise. The predictions are obtained directly by computing the distances from the test sample to the stored training data. KNN naturally adapts to non-linear decision boundaries, but its performance depends on k, feature scaling, and distance metric. We use cross-validation to obtain an optimal $k=19$ for our data.

We note that KNN is excluded from the CP analysis in Appendix B 1: its discrete output probabilities (fractions of k neighbours) hinder the ranking required by the CP algorithm, producing plateaued confidence values. It is therefore only compared via the ROC curve.

d. *XGBoost*

XGBoost (eXtreme Gradient Boosting) [66] is a gradient-boosted decision tree ensemble, where the input feature vector $\vec{X}$ is passed through a series of M decision trees $f_m(\vec{X};\lambda_m)$, each trained sequentially to correct the residual errors of the previous trees. The final model output is a sum over all trees, converted to a

probability via the sigmoid function $P_{y=1}(\vec{X};\lambda) = \sigma(z)$, with

$$z = \sum_{m=1}^{M} f_m(\vec{X};\lambda_m)\,, \tag{A6}$$

where λ_m represents the parameters of tree m, including the split features, split thresholds, and leaf weights.

Each tree f_m is constructed by recursively splitting the training data to minimise a regularised objective function, which for binary classification consists of the logistic (log-loss) term (analogous to Eq. (A1)) plus a penalty on the complexity of the tree, using the sum of squared leaf weights. The tree is constructed to fit the negative gradient of the loss (the residuals) from the current ensemble of previous trees, effectively performing a step of functional gradient descent. This sequential process allows each new tree to focus on the errors made by the current model, gradually improving predictive performance.

Regularisation parameters, including the learning rate and maximum tree depth, are used to prevent overfitting and control model complexity. XGBoost can capture complex, non-linear interactions between features and generally achieves high predictive performance [66].

The nature of decision trees means that missing (NaN) values can be handled, and it is thus not necessary to replace non-detections by zero for the XGBoost classifier. However, for comparability between classifiers, we replace non-detections with zero for XGBoost as well. We implement XGBoost using the `XGBoost` package and, using cross-validated grid-search, obtain the optimal classifier with 96 trees and a maximum depth of 6.

3. Conformal prediction

CP [45, 46] is a framework developed to provide statistically rigorous and well-calibrated uncertainties for any point prediction. CP does not modify the underlying algorithm but instead uses its predictions on a labelled calibration dataset to learn the uncertainty. Thus, CP requires no assumptions about the model or data distributions. The only requirement is that the data are exchangeable.

First, a nonconformity measure $A(\vec{X}, y)$ is defined to quantify how unusual a sample-label pair $(\vec{X}, y)$ is, with smaller values indicating better agreement with the model. The choice of nonconformity measure depends on the problem (see Malz et al. [55] for discussion), and here we define it as the complement of the classifier prediction probability,

$$A(\vec{X}, y) = 1 - P_y(\vec{X};\lambda)\,, \tag{A7}$$

where $P_y(\vec{X};\lambda) \in [0,1]$ is the classification score for label y.

In this work, we employ Mondrian (label-conditional) CP [67, 93] to guarantee conditional coverage for each class. During calibration, for each label, a nonconformity score $s_n^y = A(\vec{X}_n, y)$ is computed for each feature vector $\vec{X}_n$ in the calibration dataset. The scores are then sorted in ascending order, and the per-label $(1-\alpha)$ quantile is obtained as

$$\hat{q}_y = s^y_{\lceil (N_y+1)(1-\alpha)\rceil}\,, \tag{A8}$$

where $\alpha \in [0,1]$ is the user-chosen error rate and N_y is the number of data points in the calibration data of label y.

For a new test sample $\vec{X}'$, the nonconformity scores $A(\vec{X}', y)$ are computed for all possible labels y. A prediction set Γ^α is then defined as containing all labels (signal and noise, in our binary case) whose nonconformity score falls at or below the $(1-\alpha)$ quantile of the calibration scores for that label:

$$\Gamma^\alpha = \{y : A(\vec{X}', y) \leq \hat{q}_y\}\,. \tag{A9}$$

CP guarantees that, in the limit of a large calibration set, the true label Y' is included in the prediction set Γ^α with probability approximately $1-\alpha$. More formally, for a finite calibration set of size N_y per label:

$$1-\alpha \leq \Pr(Y' \in \Gamma^\alpha(\vec{X}')|Y' = y) \leq 1-\alpha+\frac{1}{N_y+1}\,. \tag{A10}$$

By using Mondrian CP, we ensure conditional coverage for each class individually, in addition to marginal coverage across the entire dataset.

To quantify the significance of individual events, we use the conditional confidence in the signal label, defined as the largest value of α for which the signal label is included in the prediction set Γ^α [47]. Formally, since $\Gamma^{\alpha=0}(\vec{X})$ contains all labels by construction, this maximum is always well-defined:

$$\texttt{conf}_{y=1}(\vec{X}) = \max\left\{\alpha \in [0,1] : y = 1 \in \Gamma^\alpha(\vec{X})\right\}\,. \tag{A11}$$

In practice, we evaluate Γ^α over a discrete grid of decreasing α values, taking the largest α for which $y = 1 \in \Gamma^\alpha(\vec{X})$ as the conditional confidence. By placing a threshold on the confidence (e.g. 0.5), a catalogue with well-defined purity can be constructed.

Appendix B: Classifier evaluation: full results

In this Section, we compare the performance of the ML classifiers introduced in Appendix A 2 to assess whether the pipeline combination framework is effective and whether results are robust to the choice of classifier. We evaluate each classifier using ROC curves and sensitivity and precision metrics under CP, and examine whether our framework produces consistent results.

1. Model comparison

The raw ML classifier output lacks a statistically rigorous significance measure, unlike the FAR provided by the maximum-$\log_{10}$IFAR approach, an essential component for assessing the significance of individual candidate events and motivating the use of CP. We therefore apply CP to the ML classifier predictions and use the conditional confidence as our significance measure for each candidate.

We apply CP to each classifier in turn, with the exception of KNN: its discrete classification probabilities hinder ranking in the CP algorithm, leading to plateaued confidence values. Increasing k removes the plateau but reduces the AUC significantly and introduces a large number of false positives. In figures where showing all classifiers would be redundant, we use XGBoost as a representative example, chosen due to its superior AUC. As a tree-based ensemble, XGBoost exhibits higher model variance than LR or MLP, with small changes in training data potentially affecting split points and tree structure; this becomes apparent when comparing results across datasets.

Using the MDC data, we calculate the conditional confidence and compare the resulting predictions to those from the maximum-$\log_{10}$IFAR method, as shown in Fig. 13. The confidence scores are broadly consistent with the maximum-$\log_{10}$IFAR ranking. At a confidence threshold of 0.5 (see Appendix B 3 for discussion), the CP method produces no false positives, compared to one for the maximum-$\log_{10}$IFAR method at the standard FAR threshold of 1 per year. The hard cut-off at the lower end of the IFAR axis reflects the 1-hour IFAR noise threshold (see Appendix A 1), below which no candidates are retained. The plot presents results for XGBoost, but we note that all classifiers exhibit similar agreement with the maximum-$\log_{10}$IFAR method.

To provide a quantitative summary of classifier performance, the number of true positive (TP), false positive (FP), false negative (FN) and true negative (TN) for each classifier are shown in Table III, along with that for the maximum-$\log_{10}$IFAR method. LR and XGBoost achieve zero FPs, while MLP and the maximum-$\log_{10}$IFAR method each produce one. The number of TP is marginally higher for the ML classifiers ($\sim 52-53\%$) than for maximum-$\log_{10}$IFAR (51%), though the differences are small. This confirms that all methods perform comparably on the mock data, with minimal false positives.

Having established that the conditional confidence behaves consistently on the mock data, we apply our combination approach to real events from the third observing run [39, 56]. In Fig. 14, we compare the resulting confidence scores with the corresponding maximum-$p_{\rm astro}$, analogous to the comparison shown in Fig. 1 for the LR classifier. Most candidates are found in the top-right and bottom-left quadrants, indicating agreement between the confidence and maximum-$p_{\rm astro}$ estimates for signals and noise, respectively.

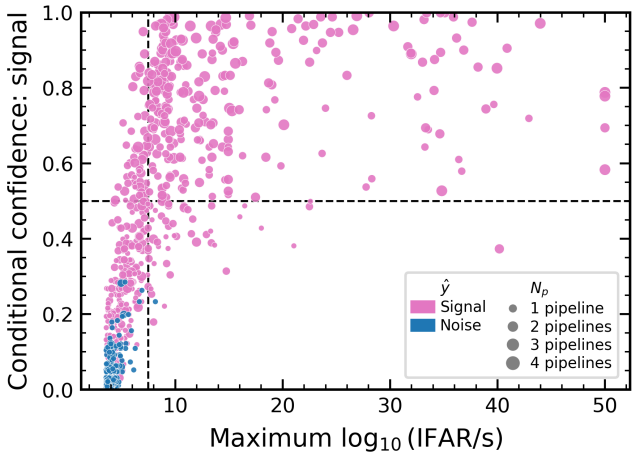


FIG. 13. The conditional confidence in the signal label for the XGBoost classifier compared to the maximum IFAR. The dashed lines show the chosen confidence threshold of 0.5 and the commonly used FAR threshold of 1 per year. The colour of each point indicates the true label $\hat{y}$, while the size indicates the number of pipelines N_p which detected an event.

TABLE III. Performance of the different classifiers + CP and the maximum-$\log_{10}$IFAR method on the MDC dataset. A threshold of 0.5 on the conditional confidence is applied for the ML classifiers and a FAR of 1 per year for the maximum-$\log_{10}$IFAR.

Method	TP	FP	FN	TN
LR	312	0	279	403
XGBoost	310	0	281	403
MLP	312	1	279	402
max $\log_{10}$(IFAR)	302	1	289	402

In the bottom-right quadrant, we identify candidates classified as signals according to their $p_{\rm astro}$ but assigned sub-threshold confidence values. As in Fig. 1, the majority of these candidates are identified by only a single pipeline, most often `GstLAL` or `cWB`, as indicated by the colours of the markers. This reflects the empirical information in the training data: events seen by multiple pipelines are more likely to be astrophysical, while single-pipeline triggers are more often associated with noise or pipeline-specific artefacts. For instance, candidates identified only by `cWB` may be less likely to correspond to CBC signals, as the pipeline relies on coherence rather than a templated search. As the only pipeline configured to identify single-detector signals in O3 [39], `GstLAL` naturally reports a larger number of candidates than pipelines requiring multi-detector coincidence. We also note that many of the `GstLAL` single-pipeline candidates pass the FAR threshold. Although differences in search methods, tuning, and configurations mean that pipelines are not expected to always identify the same candidates, our framework has learned from

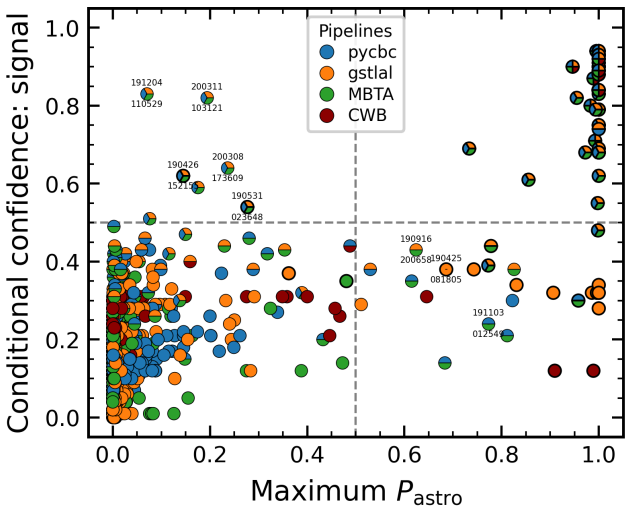


FIG. 14. The conditional confidence in the signal label for the XGBoost classifier compared to the maximum $p_{\rm astro}$ for the O3 events in the combined GWTC-2.1 and GWTC-3.0 catalogue. The classifier is trained and CP calibrated on the MDC data. The dashed lines represent the confidence and $p_{\rm astro}$ thresholds, respectively. High-significance events (FAR $<$ 1 per year) are indicated by a bold marker outline.

the training data that these single-pipeline events are statistically less likely to be astrophysical signals.

A notable example among the down-ranked single-pipeline events is GW190425_081805, a single-detector BNS identified only by `GstLAL` with a $p_{\rm astro}$ of 0.69 in O3 [56, 57]. Its total mass of $\sim 3.4\,M_\odot$ exceeds that of all known galactic BNS systems, and GW data cannot rule out the possibility that one or both components of the system are black holes [57].

There are also two three-pipeline and nine two-pipeline candidates in this quadrant. Notably, both three-pipeline candidates are high-significance events (FAR $<$ 1 per year), suggesting that the XGBoost classifier is penalising some aspect of their feature distribution beyond raw significance.

In the top-left quadrant, we identify several events with sub-threshold $p_{\rm astro}$ values but conditional confidence scores exceeding the threshold, all detected by three pipelines each. We find that XGBoost independently recovers several candidates previously up-ranked by LR in Fig. 1, lending additional weight to their potential astrophysical origin. Most notably, this includes GW200311_103121, with conditional confidence 0.82, the sub-threshold BNS candidate listed in the marginal candidate table of GWTC-3.0. Ashton and Dietrich [94] performed parameter estimation on GW200311_103121, finding source masses of $1.4M_\odot$ and $1.2M_\odot$ and concluded that "analysing the event under the assumption that it is an astrophysical signal, its properties are highly consistent with that of a binary neutron star merger".

We also find GW190426_152155 and GW190531_023648, two marginal significance NSBH candidates in the GWTC-2.1 catalogue [56], which were also up-ranked by LR in Fig. 1. Both candidates pass the FAR threshold in the `GstLAL` pipeline (with 0.91 yr^{-1} and 0.41 yr^{-1}, respectively), but obtain low $p_{\rm astro}$ values of 0.14 and 0.28.

Furthermore, XGBoost also up-ranks GW200308_173609 and GW191204_110529, two BBH candidates with maximum-$p_{\rm astro}$ of 0.24 in `MBTA`, and 0.07 in `GstLAL`, respectively, but with conditional confidences of 0.64 and 0.83. Notably, both of these events are also detected by the `PyCBC`-BBH search with a $p_{\rm astro}$ of 0.86 and 0.74, respectively, but these results are excluded from our test data set for exchangeability reasons previously discussed. These cases illustrate an important consistency check: our framework independently up-ranks events that a separate, excluded pipeline search also considers significant, providing an external validation of the up-rankings.

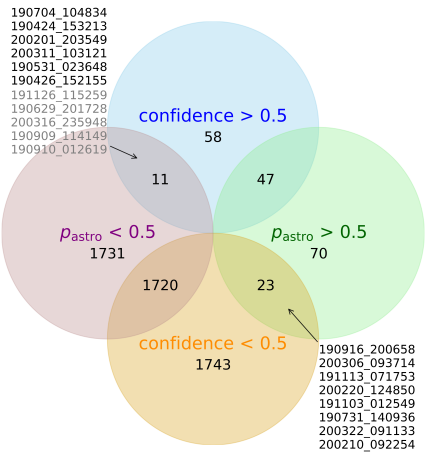
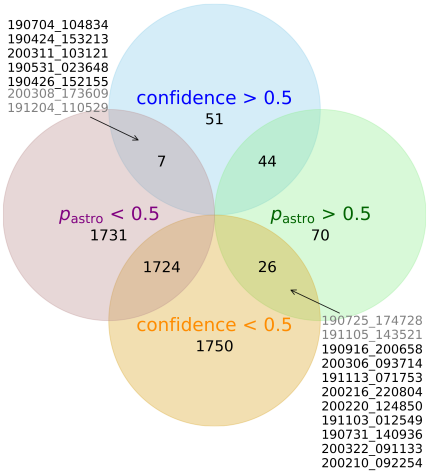
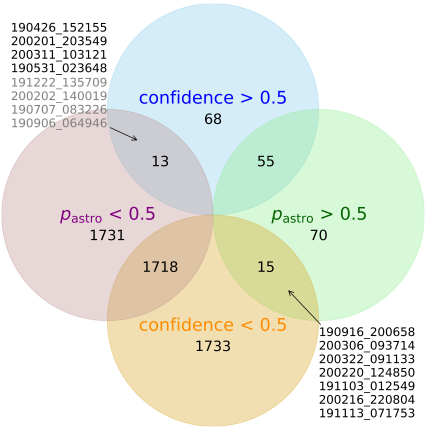
To assess the consistency of results across classifiers, we construct summary plots representing the different regions in the $p_{\rm astro}$ versus conditional confidence plots. Table IV shows these diagrams for the LR, MLP, and XGBoost classifiers. The diagrams indicate the number of events in each region, and highlight multi-pipeline events where the confidence and $p_{\rm astro}$ statistics disagree. Events annotated in black appear in the same quadrant for two or more classifiers, indicating consistent classification.

From Table IV, we find that GW200311_103121, GW190426_152155 and GW190531_023648 consistently have confidence values above threshold for all classifiers. This demonstrates robustness and consistency; multiple classifiers independently assigning high confidence to the same sub-threshold candidate increases the reliability of the prediction. Notably, these candidates correspond, if real, to a BNS and two NSBH systems.

The low $p_{\rm astro}$ values of these candidates reflect the known population uncertainties discussed in Abbott et al. [39]. While the BBH mass distribution is now relatively well constrained, the BNS and NSBH populations remain poorly characterised, leading to larger uncertainties in the astrophysical prior used to compute $p_{\rm astro}$. For such systems, these uncertainties can exceed 0.1 in $p_{\rm astro}$ for candidates near the detection threshold, meaning that $p_{\rm astro}$ values may be particularly sensitive to assumptions about the underlying population [39]. Additionally, the higher detectable BBH merger rate means BBH candidates receive higher $p_{\rm astro}$ values than low-mass systems at comparable FAR, causing $p_{\rm astro}$-based thresholds to preferentially exclude BNS and NSBH candidates.

This behaviour is illustrated by GW190426_152155, which was included as a confident candidate in GWTC-2.0 under the FAR $<$ 2 yr^{-1} detection criterion [95], but was reclassified as a marginal candidate in GWTC-2.1 which uses $p_{\rm astro} \geq 0.5$ as the detection threshold [56]. Notably, GWTC-2.0 did not assign a $p_{\rm astro}$ to this event, citing strong prior dependence on assumed NSBH signal

TABLE IV. Comparison of the three ML classifiers on GWTC-3.0 data. Events in regions where the confidence and $p_{\rm astro}$ disagree are annotated if detected by more than one pipeline. Events where two or more classifiers agree are annotated in black, while events unique to that classifier are shown in grey.

LR	**XGBoost**	**MLP**
		

rates. GWTC-2.1 subsequently estimated a low $p_{\rm astro}$ of $p_{\rm NSBH} = 0.14$ [56], reflecting the lower inferred rate of detectable NSBH mergers rather than weak search significance (FAR of 0.91 $\rm yr^{-1}$). In contrast, our framework relies primarily on empirical multi-pipeline information rather than population modelling. A dedicated reanalysis of GW190426_152155 found it to be consistent with either an NSBH merger or a low-mass BBH [96]. The consistent up-ranking of these BNS and NSBH candidates across all classifiers therefore suggests coherent support from multiple search pipelines that is not fully captured by current population-informed $p_{\rm astro}$ estimates.

While XGBoost up-ranks only a few events, LR and MLP up-rank considerably more candidates. For LR, these are all three-pipeline events, consistent with XGBoost. MLP, however, also up-ranks several single- and two-pipeline candidates, suggesting it is less conservative than the other classifiers, which we discuss further in later sections.

Similarly to GW200308_173609 and GW191204_110529 (up-ranked by XGBoost), GW191126_115259 (up-ranked by LR) was also detected by the `PyCBC`-BBH search with a $p_{\rm astro}$ of 0.7. GW200201_203549, up-ranked by both LR and MLP, is (if real) another NSBH low-$p_{\rm astro}$ candidate that appears in the marginal candidate table of GWTC-3.0 [39].

Although these events are not yet confirmable as astrophysical signals, these results illustrate the potential of pipeline combination to identify sub-threshold candidates that other methods may overlook; such identifications may become more reliable with improved control over systematic differences.

There are six multi-pipeline events with $p_{\rm astro} \geq 0.5$ but confidence < 0.5 for all classifiers, all of which are two-pipeline candidates with low significance. GW191103_012549 and GW190916_200658 are BBH candidates identified with a maximum-$p_{\rm astro}$ in `PyCBC` and `MBTA`, respectively, but the highest $p_{\rm astro}$ was obtained by `PyCBC`-BBH, which is excluded from our test data (as discussed in Appendix A 1). The other four events, which are consistently down-ranked, have a $p_{\rm astro} \geq 0.5$ in the `MBTA` pipeline only. In addition, all of them were also seen by the `PyCBC`-BBH search (albeit with small $p_{\rm astro}$). Furthermore, there are four multi-pipeline high significance events which are down-ranked; all are down-ranked by XGBoost, while LR and MLP each independently down-rank one candidate from this group.

Overall, the three classifiers show broad agreement on which events to up-rank and down-rank, with differences arising primarily from XGBoost being more conservative. XGBoost achieves the highest AUC and is the most conservative classifier, up-ranking only events with strong multi-pipeline support, while also down-ranking more events than the other classifiers. LR performs comparably and up-ranks a similar set of three-pipeline candidates but down-ranks fewer events than XGBoost. MLP is the least conservative, up-ranking the most candidates, including single- and two-pipeline events, and down-ranking the fewest events.

A full list of confidence scores for all ML classifiers and $p_{\rm astro}$ values for all events in the GWTC-3.0 catalogue where the maximum-$\log_{10}$IFAR method disagrees with our framework is included in Appendix C.

2. Sensitivity and precision

In the GW literature, the sensitive volume [23, 97] is a key metric used to compare pipeline performance on mock

data. It is estimated from injections as the fraction of simulated signals recovered above a given FAR threshold (equivalently, the sensitivity at that threshold) scaled by the maximum survey volume [23, 97]. Since sensitive volume is directly proportional to sensitivity at a fixed threshold, we consider the latter first. Sensitivity, also referred to as recall or true positive rate, is the fraction of true events correctly identified as signals and is formally defined as

$$\texttt{sensitivity} = \frac{\mathrm{TP}}{\mathrm{TP} + \mathrm{FN}}\,, \tag{B1}$$

where TP is the number of events correctly predicted as signals and FN the number incorrectly predicted as noise. By this definition, a high sensitivity can be achieved even if many noise triggers are misclassified as signals, since FPs are not accounted for. Precision complements sensitivity by quantifying how reliable the detections are, and is defined as the fraction of positive predictions that are true signals,

$$\texttt{precision} = \frac{\mathrm{TP}}{\mathrm{TP} + \mathrm{FP}}\,. \tag{B2}$$

Together, these metrics provide a more complete picture of classifier performance than the ROC curve alone, which is insensitive to class imbalance and does not directly account for precision [98, 99]. In real GW searches, noise candidates vastly outnumber signals, making precision particularly informative. However, the MDC dataset has an artificially high signal rate, so the precision values reported here should be interpreted accordingly.

For our pipeline combination approach, however, the sensitivity curve computed by varying the detection threshold is necessarily diagonal. This arises from the validity guarantee of CP and the conditional confidence definition chosen. CP guarantees that the true label is included in the prediction set Γ^α with a probability of approximately $1-\alpha$ (see Eq. (A10)). Using Mondrian (label-conditional) CP, we can make this guarantee for each class (signal or noise) individually. Thus, by varying the threshold α, CP guarantees an approximately diagonal coverage (sensitivity) curve when the calibration set is sufficiently large. Because the conditional confidence used to assess the significance of each candidate corresponds to the value of α at which the signal label is included in the prediction set, the resulting plot of sensitivity versus confidence is also necessarily diagonal. This is illustrated in Fig. 15; all methods that include CP yield a diagonal sensitivity curve.

A direct comparison with the maximum-$\log_{10}$IFAR curve is not straightforward, as the threshold scales non-linearly. Instead, we include the maximum-p_{astro} for a rough comparison, while noting that the p_{astro} values in the MDC dataset are not physically realistic since the enhanced signal rate of the dataset means the p_{astro} is not well calibrated [63].

Therefore, to make a fair comparison, we apply CP to the maximum-$\log_{10}$IFAR and maximum-p_{astro} as well, ensuring all approaches are evaluated under the same framework. Applying CP does not affect the underlying ranking of events, but converts the raw significance measure into a calibrated confidence value on the same $[0, 1]$ scale as the ML classifiers, enabling a direct comparison at a common threshold.

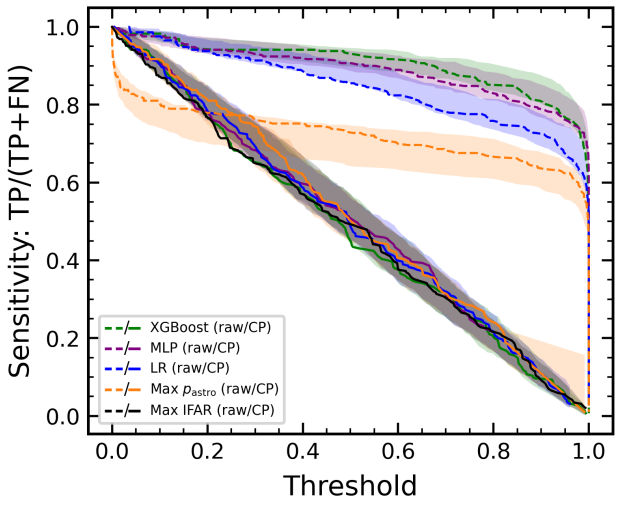


FIG. 15. Sensitivity for the LR and XGBoost classifiers trained and evaluated on the MDC data. Dashed lines represent methods with CP applied. The maximum-$\log_{10}$IFAR and maximum-p_{astro} methods with CP applied are also shown for comparison. The shaded bands show the 90% confidence interval over 100 permutations of data splits, while the lines illustrate one of the realisations.

This diagonal behaviour also implies that sensitive volume would be identical across all CP-calibrated classifiers, rendering it uninformative for comparison.

While the sensitivity plot in Fig. 15 is not informative for comparing the performance of different methods, the precision plot in Fig. 16 provides a more meaningful assessment of how reliably each method identifies true signals. The figure shows the precision curves for the ML classifiers, both with and without the application of CP, along with the maximum-$\log_{10}$IFAR and p_{astro} methods, each with CP applied.

We observe that for the ML classifiers shown, applying CP increases the precision significantly. All ML classifiers also perform better than the maximum-$\log_{10}$IFAR method. For the maximum-p_{astro}, applying CP appears to increase the precision only for threshold values above ~ 0.3. However, this might be an artefact of the physically unrealistic p_{astro}.

By construction, CP precision approaches one at high confidence thresholds, since events assigned high confidence are very likely to carry the signal label as their true class.

We can also plot the ROC and the precision-sensitivity curves, using the CP confidence as threshold, and calculate the AUC for both, see Fig. 17 and Fig. 18 respectively.

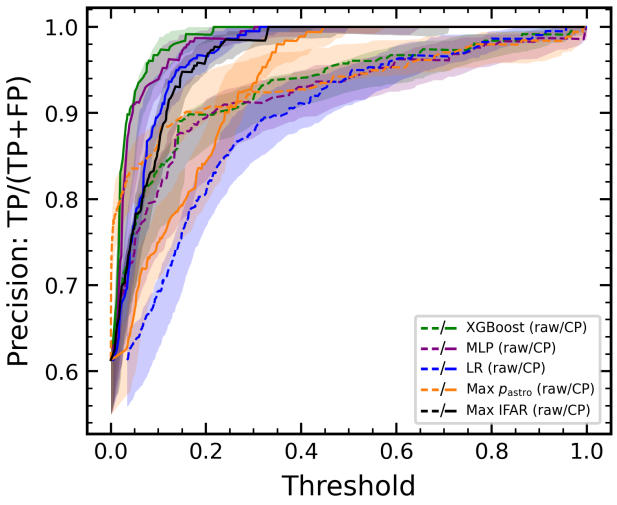


FIG. 16. Precision curves for the LR and XGBoost classifiers trained and evaluated on the MDC data. The dashed lines represent methods with CP applied. The maximum-$\log_{10}$IFAR and maximum-p_{astro} methods with CP applied are also shown for comparison. The shaded bands show the 90% confidence interval.

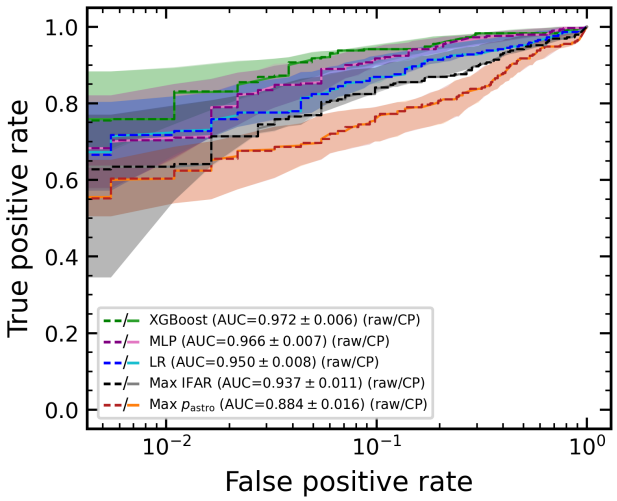


FIG. 17. ROC curves using the CP confidence as threshold. The ROC curves for the classifiers directly and the maximum-$\log_{10}$IFAR and maximum-p_{astro} methods are also included for comparison. The shaded bands show the 90% confidence interval over 100 permutations of data splits, and the AUC is given as the mean and standard deviation of the same.

For both plots we note that adding CP on top of the underlying classification method does not change the curves or AUC. This arises because both curves only depend on the ranking of scores and since CP preserves rank, its application calibrates the output but does not change the classifier performance.

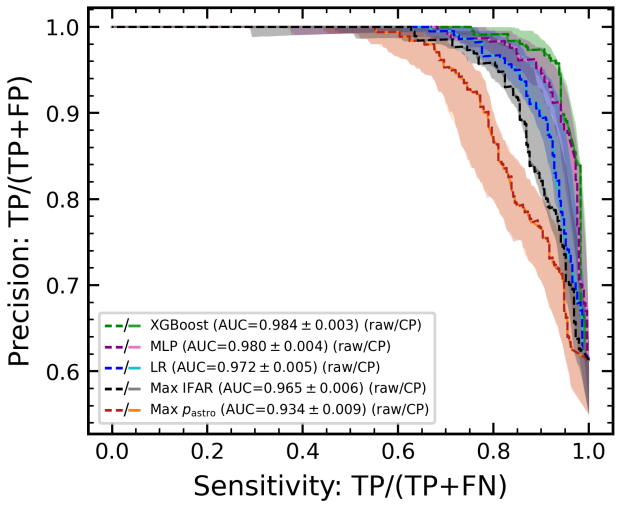


FIG. 18. Precision-sensitivity curve obtained from varying the respective thresholds for the different methods. The shaded bands show the 90% confidence interval over 100 permutations of data splits, and the AUC is given as the mean and standard deviation of the same permutation set.

In summary, the ROC curves (Figs. 2 and 17) and precision-sensitivity curve (Fig. 18) characterise overall classifier performance and are unaffected by the application of CP, which preserves rank order. The sensitivity plot (Fig. 15) is necessarily diagonal for all CP-calibrated methods and serves as a validity check rather than a discriminating metric. The precision plot (Fig. 16) is the most informative for comparing methods, showing that CP substantially improves precision for all classifiers and that all ML classifiers outperform maximum approaches.

Across all metrics, the XGBoost classifier achieves the best performance, both with and without CP applied. Combined with its conservative behaviour when assigning confidence to both mock data and real GW candidates discussed in Appendix B 1, we choose XGBoost as our preferred classifier for the remainder of this analysis.

3. Choosing the conditional confidence threshold

For our analysis so far, we have used the arbitrary confidence threshold of 0.5 to distinguish between signal and noise; we now briefly explore alternative thresholds.

If the main goal is catalogue purity, one approach to selecting a confidence threshold would be to choose the point at which precision reaches unity, ensuring no false positives. However, this threshold is highly unstable, as a single misclassified event can cause the threshold to shift dramatically. Furthermore, this approach prioritises purity at the potential expense of signal loss, and the threshold derived from mock data may not transfer reliably to real observations if detector or pipeline

characteristics differ. Nevertheless, we investigate what threshold this method would give. Over 100 permutations of the data, we obtain a conservative 95th percentile of 0.43 for XGBoost, 0.6 for LR and 0.63 for MLP.

Another approach would be to use the ROC curve. The ROC curve summarises the trade-off between true positive rate (TPR) and false positive rate (FPR) as the classification threshold is varied. A common heuristic is to minimise the Euclidean distance to the top-left corner of the ROC plane [100], $d = \sqrt{(1 - \mathrm{TPR})^2 + \mathrm{FPR}^2}$, corresponding to simultaneously high TPR and low FPR. Tsukamoto et al. [42], for example, employ this approach. While this criterion provides a simple and intuitive operating point, it implicitly assumes equal costs for false positives and false negatives and does not account for class imbalance. Moreover, the location of the optimal point can be sensitive to statistical fluctuations in finite samples. This approach should therefore be used primarily as a diagnostic tool to guide interpretation, rather than as a definitive choice for setting the final detection threshold. Using a conservative 95th percentile over 100 permutations of the data, we obtain thresholds of 0.49 for XGBoost, 0.44 for LR, and 0.39 for MLP.

Taken together, these threshold estimates cluster around values of approximately 0.5 across classifiers and selection criteria, despite considerable variability in both approaches. The two approaches yield notably different orderings across classifiers: the precision-based method assigns the lowest threshold to XGBoost and the highest to MLP, while the ROC-based method reverses this, giving XGBoost the highest and MLP the lowest. This inconsistency illustrates that neither method alone provides a stable or definitive threshold. We have therefore chosen to continue using the confidence threshold of 0.5 throughout the analysis, as it provides a simple, conservative, and broadly supported operating point without relying on unstable data-driven optimisation.

4. Feature importance

Having established XGBoost as our preferred classifier, we now examine the decision-making process of all classifiers through SHAP analysis [68], using XGBoost as the primary example. SHAP analysis quantifies the contribution of each input feature to individual predictions, revealing which pipeline outputs drove a given prediction by how much and in which direction. This allows us to move beyond black-box predictions and understand the physical reasoning behind each classification.

A natural starting point for understanding classifier decisions is to examine built-in feature importance metrics, such as coefficient magnitudes for LR or impurity-based importance for tree models. However, these global metrics reflect the influence of each feature conditional on all others, which can be misleading when features are correlated, and cannot explain how individual predictions are driven by specific feature values.

SHAP [68] addresses these limitations by providing a unified framework for feature attribution based on Shapley values from cooperative game theory. SHAP values quantify the contribution of each feature to individual predictions while accounting for feature dependencies, offering detailed insight into model behaviour and increasing model transparency and interpretability. We compute SHAP values using the `shap` Python package [68, 101].

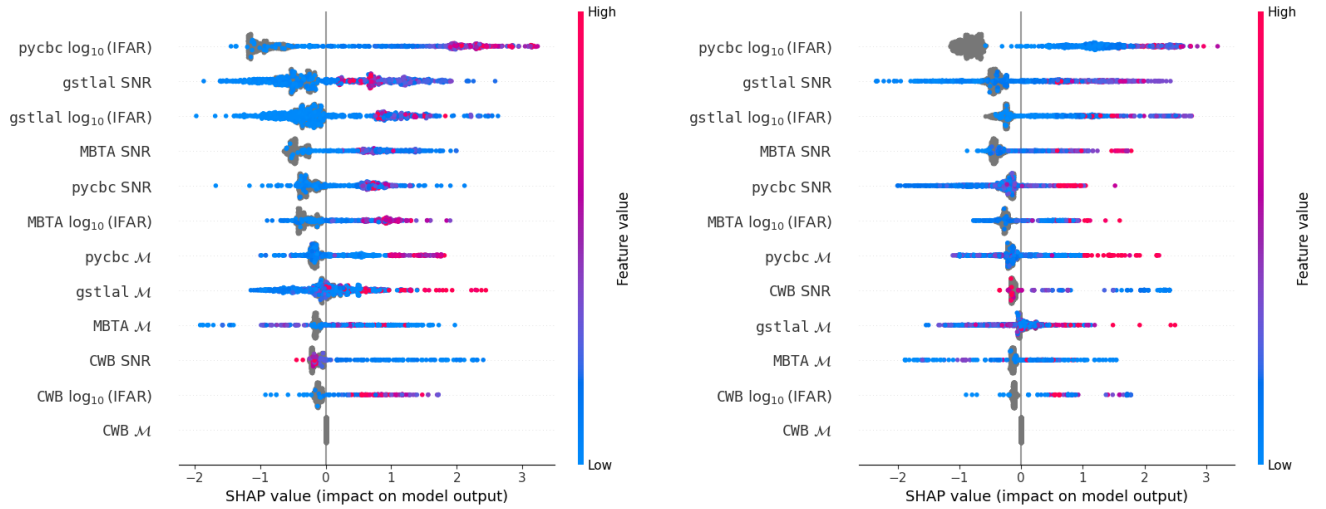
For a given prediction $f(x)$, SHAP decomposes the output into a baseline value $E[f(x)]$, the mean model output over the background dataset, plus additive feature contributions:

$$f(x) = E[f(x)] + \sum_i \phi_i \,, \tag{B3}$$

where the magnitude of each $\phi_i \in \mathbb{R}$ indicates the strength of feature i's influence, and its sign indicates the direction of effect. Each ϕ_i is computed as the weighted average marginal contribution of feature i across all possible subsets of the remaining features [68]. Global feature importance can be derived by averaging absolute SHAP values across all predictions, while individual SHAP values reveal how specific feature values influence particular predictions. We note that while SHAP values account for feature interactions in their computation, the summary plots shown do not make these interactions directly visible; dependence plots would be required to reveal such correlations.

First, we consider the global SHAP values for the XGBoost classifier applied to the MDC and O3 data, respectively, using the MDC training data as the reference baseline. The results are shown in Fig. 19, where each point represents the SHAP values for a specific feature and event in the respective dataset, coloured by the feature value. For example, high values of `PyCBC` $\log_{10}$(IFAR) influence the classifier toward a signal prediction in both datasets, whereas low or missing values (shown in grey) push the prediction toward noise. We note similar behaviour in most of the features, and observe that there is little difference between the two datasets. This similarity is expected: the MDC is constructed to mimic realistic detection scenarios, so a well-trained classifier should respond consistently to equivalent feature values regardless of whether the data are simulated or real.

The $\log_{10}$(IFAR) features from the templated pipelines dominate the ranking, with `PyCBC` $\log_{10}$(IFAR) being the single most important feature in both datasets. High values push strongly toward a signal prediction, while missing values, corresponding to non-detections, contribute a small negative score. SNR features play a secondary but consistent role, while chirp mass features rank lower, indicating that the classifier relies primarily on detection significance rather than source parameters. `cWB` features are the least influential overall, possibly due to the role as an unmodelled search. The close agreement in feature rankings and SHAP distributions between the two panels suggests that the classifier generalises well from simulated



(a) MDC

(b) GWTC-2.1 and GWTC-3.0

FIG. 19. Summary plot of the SHAP values for the MDC-trained XGBoost classifier on the MDC and O3 data in GWTC-2.1 and GWTC-3.0, respectively. The x-axis shows the SHAP values: a positive value corresponds to influence toward a signal prediction, while a negative value corresponds to influence toward a noise prediction. The magnitude indicates the strength of influence. The features are ordered by the mean absolute SHAP value across all test events, with the most influential feature at the top. The colour scale represents the value of the features, and grey points indicate missing values. Each point represents a single event, plotted at its SHAP value for the corresponding feature.

to real data.

To compare feature importance across classifiers, we show the mean SHAP values for LR, MLP, and XGBoost in Fig. 20. The plot shows the mean SHAP value for each feature, normalised by each classifier's maximum absolute mean SHAP value for a clearer cross-classifier comparison, and is thus less informative than the distribution of local values shown in Fig. 19(a) for the same data.

This also accounts for the slight discrepancy for XGBoost: by default, the features in Fig. 19 are ranked by the absolute mean SHAP value, while Fig. 20 shows the signed mean. All three classifiers agree that $\log_{10}$(IFAR) features dominate over SNR and chirp mass features, confirming that multi-pipeline detection significance is the primary driver of classification. SNR features play a more prominent secondary role for XGBoost than for LR or MLP, suggesting that XGBoost exploits non-linear interactions between significance and signal strength. `cWB` features consistently rank low across all classifiers, and the `cWB` $\log_{10}$(IFAR) carries a negative mean SHAP value for all classifiers. This is driven by non-detections: `cWB` produces a trigger for only around 26% of signals in the MDC, so the dominant value of `cWB` $\log_{10}$(IFAR) is zero, which the classifier associates with noise. A high `cWB` $\log_{10}$(IFAR) would contribute positively (as shown in Fig. 19(a)), but this is rare in the MDC, partly because 41% of injections are BNS signals that `cWB` is not well suited to detect.

We can also examine feature importance for individual events to understand the reasoning behind a specific prediction. Focusing on the up-ranked BNS candidate

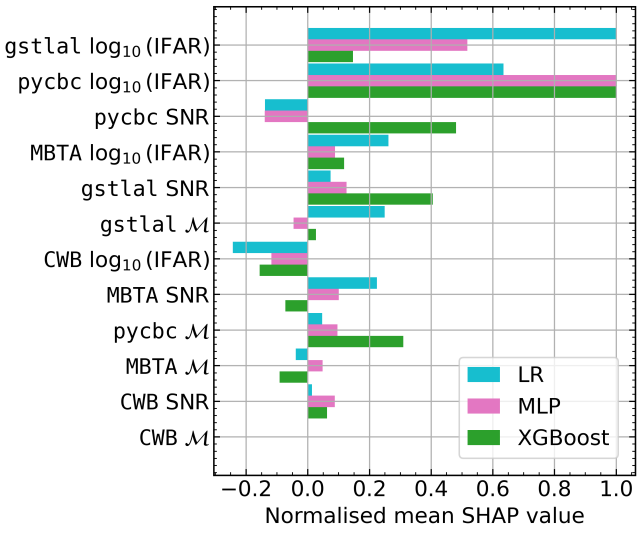


FIG. 20. Comparison of mean SHAP values for the different classifiers on the MDC data. For each classifier, the mean SHAP values are normalised by the maximum absolute mean SHAP value of that classifier, scaling each to the range $[-1, 1]$ to enable comparison across classifiers with different output scales.

GW200311_103121, the SHAP values, computed using GWTC-3.0 as the reference dataset, are shown in the waterfall plot in Fig. 21 for the XGBoost classifier. In the waterfall plot, each feature is shown on the y-axis alongside its value, with arrows indicating how much it

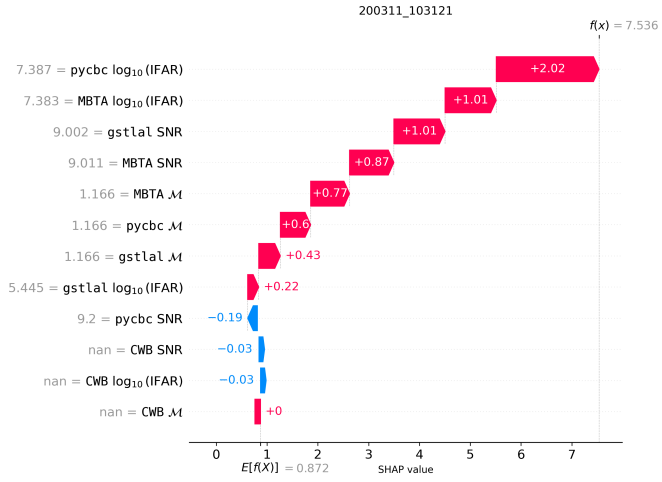


FIG. 21. SHAP waterfall plot for GW200311_103121, relative to other O3 data from GWTC-2.1 and GWTC-3.0, using XGBoost trained on the MDC. The SHAP values for each feature are represented by the arrows, where length and colour/direction indicate the magnitude and direction of the feature's influence. The model output $f(x) = 7.536$ and expected value $E[f(x)] = 0.872$, computed on the raw classifier output log-odds, correspond to probabilities $p \approx 1$ and $p \approx 0.71$, respectively.

shifts the prediction from the baseline $E[f(x)]$ (the average model output over the GWTC-3.0 data) toward the final prediction $f(x)$, where the arrow length and colour indicate magnitude and sign respectively.

The SHAP values are computed on the raw ML model output, which for the XGBoost classifier corresponds to the log-odds $f(x) = \log \frac{p}{1-p}$. While these log-odds can be converted to probabilities p, doing so means that the sum of the SHAP values no longer exactly equals the difference from the baseline, so the resulting plot provides only an approximate decomposition. In Fig. 21, we therefore show the plot in log-odds units.

The top features in Fig. 21 are the $\log_{10}$(IFAR) values from `PyCBC` and `MBTA`, with values just below the threshold of $\log_{10}(\text{IFAR}) = 7.5$ in units of seconds (corresponding to a FAR of 1 per year). An SNR of ≈ 9 from `GstLAL` and `MBTA` also influences the prediction toward being a signal, while a similar SNR from `PyCBC` appears more noise-like to the classifier. A non-detection from `cWB` leads to the `cWB` features not affecting the prediction much in any direction. The `GstLAL` $\log_{10}$(IFAR) value of 5.4 (sub-threshold) contributes only marginally, with a small positive score. Additionally, the chirp mass features from all three pipelines, each reporting $\mathcal{M} = 1.166\,M_\odot$, contribute positively to the signal prediction. This low chirp mass is consistent with a BNS system, and the classifier has evidently learned to associate such values with astrophysical signals.

For comparison, we also show waterfall plots for a confirmed 4-pipeline signal, GW191222_033537 from the GWTC-3.0 catalogue ($p_{\text{astro}} = 1$, confidence 0.97, Fig. 22(a)), and a 2-pipeline noise candidate, GW200324_081850 ($p_{\text{astro}} = 0.001$, confidence 0.13, Fig. 22(b)).

The SHAP decomposition for GW200311_103121 shares the same qualitative structure as GW191222_033537, dominated by large positive contributions from multi-pipeline $\log_{10}$(IFAR) features, supporting its classification as a genuine signal. However, the overall prediction is less decisive, reflecting lower $\log_{10}$(IFAR) values and the absence of a `cWB` detection. In contrast, the noise candidate GW200324_081850 shows positive contributions from `PyCBC` and `MBTA` $\log_{10}$(IFAR), offset by stronger negative contributions from the chirp mass and SNR features and the absence of `GstLAL`, resulting in a clear noise classification.

Overall, the SHAP analysis reveals that XGBoost's classification decisions are driven primarily by multi-pipeline detection significance, with source parameters playing a secondary role. The consistent feature rankings across classifiers and between simulated and real data demonstrate that the framework is robust and physically interpretable. The waterfall analysis for GW200311_103121 further shows that its high-confidence classification is supported by both strong multi-pipeline $\log_{10}$(IFAR) values and a chirp mass consistent with a BNS system, providing a physically coherent basis for its up-ranking.

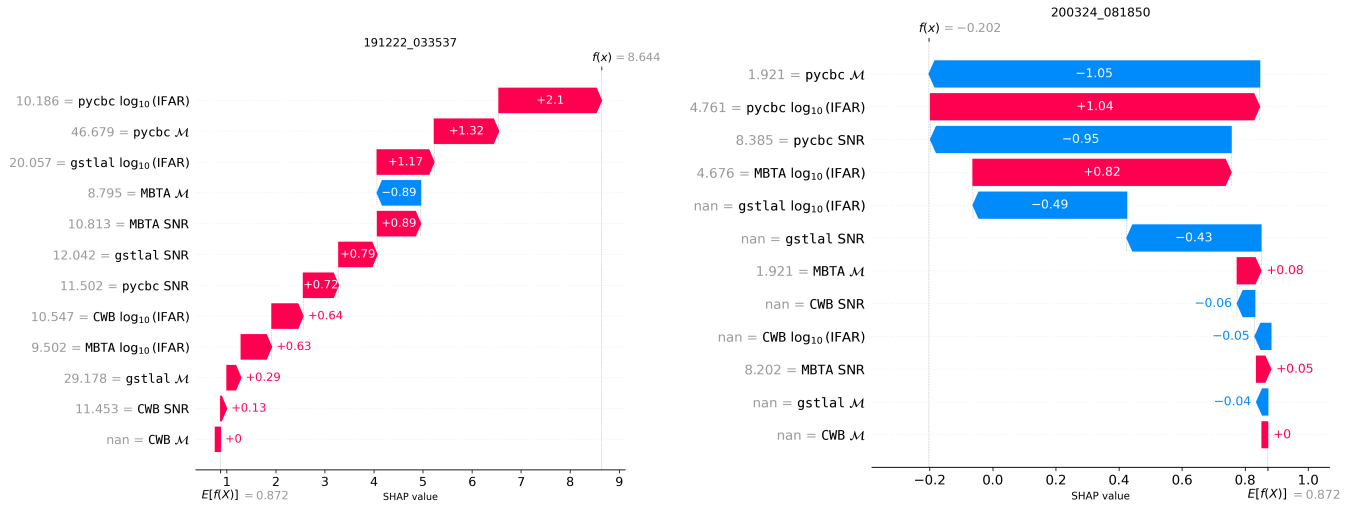
Appendix C: Tables of conditional confidence scores for candidates from O3, O4a and O4b

In Table V, Table VI, and Table VII we tabulate the up-ranked candidates from O3, O4a and O4b studied in this work, enabling a comparison of the p_{astro} and conditional confidence where they disagree.

In Table VIII, Table IX, and Table X we tabulate the down-ranked candidates from O3, O4a and O4b studied in this work, enabling a comparison of the p_{astro} and conditional confidence where they disagree.

Appendix D: Tables of posterior parameters for up-ranked events

The following tables list the median and 90% credible intervals of the posterior parameter estimates for up-ranked O4 candidates in the GWTC-4.1 (Table XI) and GWTC-5.0 (Table XII) analyses. Parameter estimation was performed using `Bilby` with the `IMRPhenomXPHM` waveform model, following the approach of GWTC-5.0 [1].



(a) GW191222_033537 (b) GW200324_081850

FIG. 22. SHAP waterfall plot for GW191222_033537 (signal) and GW200324_081850 (noise), relative to other O3 data from GWTC-2.1 and GWTC-3.0, using XGBoost trained on the MDC. The SHAP values for each feature are represented by the arrows, where length and colour/direction indicate the magnitude and direction of the feature's influence.

TABLE V. Up-ranked O3a and O3b candidates from GWTC-2.1 and GWTC-3.0. The reported chirp mass is taken from the pipeline with the maximum p_{astro} value. For `cWB`, the chirp mass is not reported, as we do not use this in our analysis.

Candidate	Data	Pipeline	$\mathcal{M}$	p_{astro}	Confidence LR	Confidence XGBoost	Confidence MLP
GW190424_153213	O3a	`MBTA`	3.5	0.076	0.600	0.510	0.480
GW190426_152155	O3a	`GstLAL`	2.6	0.145	0.610	0.620	0.630
GW190531_023648	O3a	`GstLAL`	2.0	0.277	0.630	0.540	0.650
GW190629_201728	O3a	`MBTA`	3.9	0.006	0.520	0.320	0.390
GW190704_104834	O3a	`PyCBC`	4.6	0.175	0.560	0.590	0.480
GW190707_083226	O3a	`cWB`	-	0.159	0.400	0.400	0.580
GW190906_064946	O3a	`PyCBC`	4.4	0.099	0.400	0.380	0.500
GW190909_114149	O3a	`PyCBC`	8.0	0.150	0.560	0.470	0.420
GW190910_012619	O3a	`PyCBC`	9.7	0.074	0.520	0.270	0.390
GW190913_153716	O3a	`GstLAL`	24.1	0.004	0.130	0.270	0.630
GW191114_003412	O3b	`GstLAL`	12.4	0.006	0.110	0.210	0.630
GW191126_115259	O3b	`PyCBC`	11.4	0.389	0.590	0.320	0.430
GW191204_110529	O3b	`GstLAL`	28.5	0.070	0.480	0.830	0.380
GW191222_135709	O3b	`PyCBC`	6.6	0.289	0.420	0.380	0.510
GW200105_162426	O3b	`GstLAL`	3.6	0.362	0.200	0.370	0.640
GW200201_203549	O3b	`GstLAL`	2.1	0.116	0.500	0.420	0.540
GW200202_140019	O3b	`PyCBC`	5.2	0.066	0.400	0.460	0.500
GW200221_142805	O3b	`GstLAL`	40.6	0.291	0.200	0.310	0.510
GW200229_130505	O3b	`GstLAL`	24.1	0.001	0.230	0.270	0.880
GW200308_173609	O3b	`MBTA`	45.2	0.236	0.460	0.640	0.440
GW200311_103121	O3b	`PyCBC`	1.2	0.194	0.660	0.820	0.610
GW200316_235948	O3b	`PyCBC`	5.0	0.138	0.520	0.300	0.430

TABLE VI. Up-ranked O4a candidates from GWTC-4.1. The reported chirp mass is taken from the pipeline with the maximum $p_{\rm astro}$ value. For `cWB`, the chirp mass is not reported, as we do not use this in our analysis.

Candidate	Data	Pipeline	$\mathcal{M}$	$p_{\rm astro}$	Confidence LR	Confidence XGBoost	Confidence MLP
GW230527_071259	O4a	PyCBC	51.2	0.204	0.450	0.350	0.520
GW230611_165753	O4a	GstLAL	54.1	0.078	0.320	0.170	0.890
GW230622_160042	O4a	MBTA	49.9	0.461	0.590	0.320	0.630
GW230625_063417	O4a	PyCBC	38.7	0.044	0.520	0.320	0.420
GW230625_211555	O4a	PyCBC	38.7	0.225	0.560	0.300	0.460
GW230627_114138	O4a	PyCBC	24.7	0.360	0.730	0.500	0.530
GW230719_070908	O4a	GstLAL	55.1	0.086	0.450	0.380	0.620
GW230723_125531	O4a	PyCBC	62.6	0.113	0.450	0.380	0.580
GW230812_001904	O4a	GstLAL	57.5	0.097	0.500	0.270	0.440
GW230813_144914	O4a	GstLAL	34.5	0.250	0.610	0.480	0.550
GW230824_030342	O4a	PyCBC	16.3	0.229	0.530	0.610	0.360
GW230824_134554	O4a	GstLAL	19.4	0.135	0.520	0.500	0.340
GW230826_031533	O4a	PyCBC	45.7	0.138	0.440	0.350	0.510
GW230827_143829	O4a	GstLAL	21.5	0.098	0.520	0.520	0.370
GW230830_043238	O4a	cWB	-	0.118	0.610	0.630	0.620
GW230830_055405	O4a	PyCBC	38.7	0.040	0.530	0.240	0.410
GW230906_100145	O4a	PyCBC	45.7	0.218	0.600	0.550	0.570
GW230907_064153	O4a	cWB	-	0.134	0.610	0.400	0.610
GW230910_021701	O4a	PyCBC	78.7	0.495	0.380	0.410	0.520
GW230911_134712	O4a	GstLAL	44.7	0.381	0.460	0.470	0.520
GW230915_133509	O4a	PyCBC	51.2	0.156	0.590	0.360	0.490
GW230918_050515	O4a	PyCBC	32.0	0.038	0.520	0.340	0.470
GW230925_090300	O4a	GstLAL	80.4	0.052	0.440	0.410	0.590
GW231003_101642	O4a	GstLAL	57.5	0.049	0.430	0.280	0.560
GW231008_011953	O4a	PyCBC	62.6	0.099	0.450	0.350	0.580
GW231009_081300	O4a	GstLAL	29.5	0.429	0.570	0.480	0.420
GW231029_003952	O4a	PyCBC	62.6	0.278	0.460	0.410	0.580
GW231109_175405	O4a	GstLAL	80.2	0.231	0.470	0.380	0.650
GW231110_122926	O4a	GstLAL	48.6	0.303	0.470	0.440	0.570
GW231110_171731	O4a	GstLAL	112.3	0.431	0.450	0.500	0.500
GW231128_143157	O4a	cWB	-	0.371	0.610	0.420	0.440
GW231222_175548	O4a	PyCBC	62.6	0.034	0.430	0.280	0.550
GW231222_234123	O4a	PyCBC	17.0	0.371	0.570	0.580	0.430
GW231229_133732	O4a	GstLAL	39.4	0.053	0.700	0.360	0.640
GW240101_061317	O4a	GstLAL	42.5	0.399	0.520	0.530	0.420
GW240114_225929	O4a	MBTA	70.2	0.361	0.590	0.400	0.610

TABLE VII. Up-ranked O4b candidates from GWTC-5.0. The reported chirp mass is taken from the pipeline with the maximum $p_{\rm astro}$ value. For `cWB`, the chirp mass is not reported, as we do not use this in our analysis.

Candidate	Data	Pipeline	$\mathcal{M}$	$p_{\rm astro}$	Confidence LR	Confidence XGBoost	Confidence MLP
GW240420_210120	O4b	PyCBC	27.2	0.075	0.530	0.470	0.390
GW240422_224206	O4b	PyCBC	38.7	0.056	0.520	0.350	0.450
GW240426_100722	O4b	MBTA	26.4	0.471	0.670	0.610	0.650
GW240426_151803	O4b	cWB	-	0.410	0.780	0.540	0.710
GW240430_111634	O4b	cWB	-	0.227	0.460	0.500	0.530
GW240503_233347	O4b	PyCBC	29.7	0.043	0.530	0.420	0.380
GW240506_030828	O4b	PyCBC	62.6	0.125	0.470	0.460	0.610
GW240521_071417	O4b	MBTA	14.1	0.126	0.500	0.210	0.460
GW240601_062707	O4b	PyCBC	45.7	0.304	0.460	0.390	0.530
GW240602_001317	O4b	cWB	-	0.291	0.490	0.410	0.620
GW240609_041100	O4b	PyCBC	78.7	0.114	0.510	0.440	0.660
GW240610_154921	O4b	GstLAL	52.9	0.108	0.420	0.310	0.510
GW240615_023849	O4b	GstLAL	11.4	0.112	0.520	0.260	0.370
GW240616_144806	O4b	PyCBC	38.7	0.077	0.560	0.420	0.460
GW240623_100729	O4b	PyCBC	62.6	0.035	0.430	0.220	0.520
GW240627_210521	O4b	GstLAL	83.5	0.470	0.470	0.450	0.670
GW240629_201552	O4b	PyCBC	38.7	0.230	0.450	0.520	0.490
GW240708_081052	O4b	MBTA	20.6	0.054	0.510	0.420	0.440
GW240716_012708	O4b	PyCBC	62.6	0.030	0.570	0.440	0.610
GW240828_064943	O4b	PyCBC	25.1	0.148	0.400	0.500	0.410
GW240828_085522	O4b	cWB	-	0.311	0.600	0.700	0.550
GW240829_213343	O4b	PyCBC	62.6	0.317	0.480	0.480	0.610
GW240930_141549	O4b	PyCBC	45.7	0.074	0.450	0.470	0.500
GW241001_113345	O4b	GstLAL	35.4	0.081	0.540	0.420	0.460
GW241102_010049	O4b	GstLAL	62.5	0.143	0.440	0.450	0.560
GW241102_073135	O4b	GstLAL	77.0	0.070	0.460	0.340	0.640
GW241102_084419	O4b	MBTA	11.3	0.050	0.500	0.390	0.310
GW241109_114629	O4b	PyCBC	62.6	0.010	0.430	0.280	0.500
GW241129_122622	O4b	MBTA	59.1	0.396	0.770	0.550	0.710
GW241130_134204	O4b	GstLAL	47.6	0.018	0.550	0.490	0.590
GW241202_233002	O4b	PyCBC	78.7	0.411	0.520	0.390	0.690
GW241219_151137	O4b	MBTA	27.1	0.397	0.610	0.640	0.480
GW250119_112442	O4b	MBTA	27.1	0.169	0.450	0.380	0.550

TABLE VIII. Down-ranked O3a and O3b candidates from GWTC-2.1 and GWTC-3.0. The reported chirp mass is taken from the pipeline with the maximum $p_{\rm astro}$ value. For `cWB`, the chirp mass is not reported, as we do not use this in our analysis.

Candidate	Data	Pipeline	$\mathcal{M}$	$p_{\rm astro}$	Confidence LR	Confidence XGBoost	Confidence MLP
GW190425_081805	O3a	`GstLAL`	1.5	0.686	0.220	0.380	0.660
GW190527_092055	O3a	`GstLAL`	32.9	0.831	0.220	0.340	0.370
GW190620_030421	O3a	`GstLAL`	24.0	0.986	0.250	0.320	0.570
GW190630_185205	O3a	`GstLAL`	33.6	1.000	0.420	0.280	0.840
GW190708_232457	O3a	`GstLAL`	15.4	1.000	0.280	0.320	0.700
GW190725_174728	O3a	`PyCBC`	9.6	0.958	0.560	0.300	0.500
GW190731_140936	O3a	`MBTA`	29.1	0.778	0.410	0.440	0.500
GW190804_083543	O3a	`cWB`	-	0.989	0.370	0.120	0.260
GW190910_112807	O3a	`GstLAL`	38.7	0.996	0.280	0.320	0.590
GW190916_200658	O3a	`MBTA`	57.6	0.624	0.310	0.430	0.270
GW190917_114630	O3a	`GstLAL`	4.2	0.743	0.160	0.380	0.470
GW190926_050336	O3a	`GstLAL`	11.1	0.511	0.160	0.290	0.390
GW190930_234652	O3a	`cWB`	-	0.646	0.310	0.310	0.280
GW191103_012549	O3b	`PyCBC`	10.1	0.773	0.490	0.240	0.400
GW191105_143521	O3b	`PyCBC`	9.4	0.998	0.770	0.480	0.660
GW191113_071753	O3b	`MBTA`	13.0	0.683	0.380	0.140	0.230
GW191219_163120	O3b	`PyCBC`	4.7	0.822	0.320	0.300	0.360
GW200112_155838	O3b	`GstLAL`	28.7	1.000	0.340	0.340	0.760
GW200202_154313	O3b	`GstLAL`	8.3	1.000	0.370	0.320	0.810
GW200210_092254	O3b	`PyCBC`	7.6	0.530	0.450	0.380	0.600
GW200214_224526	O3b	`cWB`	-	0.909	0.350	0.120	0.230
GW200216_220804	O3b	`GstLAL`	13.6	0.773	0.510	0.390	0.490
GW200220_124850	O3b	`MBTA`	44.3	0.826	0.310	0.380	0.210
GW200302_015811	O3b	`GstLAL`	33.4	0.906	0.230	0.320	0.450
GW200306_093714	O3b	`MBTA`	27.5	0.812	0.370	0.210	0.230
GW200322_091133	O3b	`MBTA`	24.5	0.615	0.390	0.350	0.290

TABLE IX. Down-ranked O4a candidates from GWTC-4.1. The reported chirp mass is taken from the pipeline with the maximum $p_{\rm astro}$ value. For `cWB`, the chirp mass is not reported, as we do not use this in our analysis.

Candidate	Data	Pipeline	$\mathcal{M}$	$p_{\rm astro}$	Confidence LR	Confidence XGBoost	Confidence MLP
GW230517_044807	O4a	GstLAL	133.3	0.620	0.260	0.350	0.330
GW230528_145129	O4a	GstLAL	122.0	0.502	0.250	0.380	0.320
GW230531_141100	O4a	PyCBC	51.2	0.723	0.380	0.360	0.440
GW230603_174756	O4a	PyCBC	27.2	0.789	0.470	0.340	0.400
GW230606_024545	O4a	PyCBC	38.7	0.877	0.480	0.350	0.510
GW230606_065320	O4a	GstLAL	141.2	0.636	0.270	0.310	0.330
GW230610_061439	O4a	GstLAL	218.5	0.529	0.320	0.340	0.440
GW230615_160825	O4a	GstLAL	150.4	0.758	0.440	0.430	0.540
GW230618_102550	O4a	PyCBC	78.7	0.597	0.510	0.430	0.660
GW230624_214944	O4a	PyCBC	14.9	0.737	0.440	0.590	0.500
GW230630_070659	O4a	GstLAL	251.7	0.958	0.370	0.350	0.580
GW230702_162025	O4a	MBTA	18.9	0.603	0.410	0.410	0.390
GW230706_104333	O4a	PyCBC	15.4	0.986	0.540	0.460	0.660
GW230717_102139	O4a	PyCBC	31.8	0.673	0.620	0.520	0.470
GW230721_222634	O4a	MBTA	62.2	0.726	0.400	0.250	0.370
GW230723_084820	O4a	cWB	-	0.645	0.290	0.320	0.260
GW230728_083628	O4a	GstLAL	136.8	0.891	0.290	0.310	0.380
GW230729_082317	O4a	GstLAL	10.9	0.983	0.480	0.430	0.640
GW230807_205045	O4a	GstLAL	93.0	0.816	0.450	0.410	0.520
GW230823_142524	O4a	MBTA	42.4	0.859	0.480	0.560	0.460
GW230824_135331	O4a	cWB	-	0.583	0.270	0.300	0.230
GW230830_064744	O4a	GstLAL	34.5	0.798	0.170	0.260	0.290
GW230831_134621	O4a	PyCBC	10.5	0.800	0.630	0.440	0.520
GW230902_122814	O4a	MBTA	17.7	0.838	0.420	0.240	0.320
GW230902_150325	O4a	GstLAL	156.8	0.651	0.270	0.290	0.370
GW230902_172430	O4a	PyCBC	10.7	0.600	0.580	0.350	0.420
GW230902_224555	O4a	PyCBC	62.6	0.514	0.490	0.400	0.620
GW230904_152545	O4a	PyCBC	2.8	0.746	0.480	0.340	0.440
GW230920_064709	O4a	PyCBC	4.3	0.789	0.590	0.460	0.510
GW230925_143957	O4a	MBTA	18.9	0.550	0.430	0.200	0.310
GW231004_232346	O4a	cWB	-	0.967	0.510	0.440	0.580
GW231005_144455	O4a	PyCBC	51.2	0.515	0.360	0.360	0.420
GW231007_134720	O4a	GstLAL	32.8	0.626	0.150	0.230	0.240
GW231013_135504	O4a	PyCBC	4.3	0.530	0.300	0.260	0.300
GW231018_233037	O4a	MBTA	10.2	0.927	0.610	0.410	0.440
GW231024_023603	O4a	GstLAL	83.5	0.511	0.210	0.230	0.300
GW231025_142306	O4a	GstLAL	47.6	0.713	0.390	0.480	0.430
GW231029_111508	O4a	GstLAL	91.0	1.000	0.360	0.260	0.610
GW231102_052214	O4a	MBTA	11.0	0.719	0.430	0.150	0.310
GW231102_232433	O4a	MBTA	67.4	0.800	0.200	0.170	0.270
GW231113_112825	O4a	GstLAL	58.7	0.513	0.170	0.220	0.260
GW231204_090648	O4a	GstLAL	147.1	0.784	0.270	0.410	0.380
GW231223_075055	O4a	PyCBC	9.3	0.981	0.710	0.470	0.630
GW231230_170116	O4a	cWB	-	0.965	0.470	0.410	0.480
GW240105_151143	O4a	PyCBC	6.0	0.745	0.280	0.360	0.390

TABLE X. Down-ranked O4b candidates from GWTC-5.0. The reported chirp mass is taken from the pipeline with the maximum $p_{\rm astro}$ value. For `cWB`, the chirp mass is not reported, as we do not use this in our analysis.

Candidate	Data	Pipeline	$\mathcal{M}$	$p_{\rm astro}$	Confidence LR	Confidence XGBoost	Confidence MLP
GW240407_214946	O4b	PyCBC	62.6	0.793	0.380	0.360	0.480
GW240408_081753	O4b	MBTA	43.1	0.613	0.210	0.150	0.220
GW240411_074140	O4b	MBTA	48.2	0.678	0.420	0.350	0.390
GW240419_041206	O4b	cWB	-	0.714	0.290	0.290	0.250
GW240421_052935	O4b	cWB	-	0.774	0.470	0.420	0.510
GW240426_085802	O4b	MBTA	62.2	0.626	0.620	0.480	0.640
GW240509_102351	O4b	PyCBC	14.8	0.893	0.350	0.360	0.380
GW240512_051606	O4b	MBTA	6.5	0.697	0.250	0.250	0.270
GW240516_041939	O4b	MBTA	9.9	0.672	0.240	0.100	0.240
GW240525_201644	O4b	GstLAL	30.4	0.806	0.470	0.530	0.580
GW240526_093944	O4b	MBTA	13.0	0.971	0.280	0.190	0.300
GW240527_150907	O4b	GstLAL	163.5	0.812	0.300	0.280	0.400
GW240613_011503	O4b	GstLAL	30.7	0.738	0.160	0.250	0.270
GW240619_212357	O4b	GstLAL	39.4	0.508	0.380	0.530	0.420
GW240621_103457	O4b	GstLAL	58.5	0.505	0.560	0.410	0.530
GW240625_073331	O4b	MBTA	25.3	0.641	0.250	0.300	0.230
GW240630_212937	O4b	PyCBC	32.0	0.750	0.450	0.350	0.460
GW240701_011640	O4b	PyCBC	26.5	0.514	0.330	0.360	0.350
GW240701_013826	O4b	MBTA	52.6	0.642	0.230	0.350	0.300
GW240701_203807	O4b	GstLAL	87.3	0.547	0.620	0.410	0.750
GW240703_191355	O4b	GstLAL	36.3	1.000	0.700	0.470	0.820
GW240807_214559	O4b	PyCBC	10.0	0.660	0.400	0.310	0.440
GW240813_034548	O4b	PyCBC	10.3	0.638	0.400	0.340	0.430
GW240814_145043	O4b	MBTA	10.8	0.743	0.620	0.440	0.480
GW240828_102340	O4b	MBTA	72.8	0.621	0.610	0.490	0.720
GW240907_121650	O4b	MBTA	2.7	0.521	0.240	0.280	0.280
GW240908_174149	O4b	MBTA	7.6	0.668	0.250	0.130	0.260
GW240913_111216	O4b	GstLAL	80.4	0.617	0.220	0.240	0.300
GW240919_215453	O4b	cWB	-	0.701	0.280	0.270	0.210
GW240923_000715	O4b	MBTA	52.6	0.783	0.240	0.350	0.310
GW240923_110846	O4b	PyCBC	23.0	0.605	0.330	0.360	0.360
GW240925_000956	O4b	GstLAL	36.3	0.605	0.160	0.260	0.270
GW240930_123408	O4b	PyCBC	15.4	0.809	0.600	0.300	0.410
GW240930_234614	O4b	cWB	-	0.976	0.340	0.190	0.250
GW241018_235402	O4b	PyCBC	19.0	0.983	0.360	0.420	0.400
GW241106_110932	O4b	GstLAL	121.9	0.725	0.450	0.420	0.500
GW241109_005349	O4b	cWB	-	0.560	0.270	0.220	0.210
GW241129_140416	O4b	PyCBC	11.7	0.509	0.310	0.220	0.300
GW241201_142737	O4b	PyCBC	51.2	0.661	0.490	0.430	0.580
GW241220_062146	O4b	PyCBC	16.4	0.567	0.320	0.360	0.330
GW241230_084504	O4b	GstLAL	50.6	1.000	0.390	0.350	0.750
GW241230_233618	O4b	GstLAL	64.7	0.947	0.490	0.390	0.570
GW250105_134047	O4b	GstLAL	83.8	0.507	0.410	0.310	0.430
GW250109_083206	O4b	PyCBC	9.2	0.998	0.350	0.380	0.410
GW250116_015318	O4b	PyCBC	45.7	0.992	0.700	0.390	0.620
GW250116_051426	O4b	MBTA	62.2	0.630	0.640	0.410	0.720

TABLE XI. Median and 90% credible intervals of the posteriors for up-ranked O4a candidates in GWTC-4.1. The parameters shows are the source-frame chirp mass $\mathcal{M}$, mass ratio q, the source-frame component masses m_1 and m_2, effective inspiral spin $\chi_{\rm eff}$, effective precession spin $\chi_{\rm p}$, source inclination angle θ_{JN}, and luminosity distance D_L.

Candidate	$\mathcal{M}$ $[M_\odot]$	m_1 $[M_\odot]$	m_2 $[M_\odot]$	q	$\chi_{\rm eff}$	χ_p	θ_{JN}	d_L [Gpc]
GW230627_114138	$17.12^{+4.07}_{-3.03}$	$25.46^{+11.49}_{-6.94}$	$15.60^{+5.42}_{-4.54}$	$0.62^{+0.33}_{-0.29}$	$0.32^{+0.29}_{-0.32}$	$0.51^{+0.33}_{-0.31}$	$0.95^{+1.91}_{-0.71}$	$4.50^{+2.92}_{-2.13}$
GW230824_030342	$11.71^{+2.01}_{-1.52}$	$15.61^{+4.72}_{-2.89}$	$11.85^{+2.90}_{-2.95}$	$0.78^{+0.20}_{-0.30}$	$0.02^{+0.14}_{-0.13}$	$0.41^{+0.42}_{-0.30}$	$2.43^{+0.54}_{-2.12}$	$2.39^{+1.76}_{-1.23}$
GW230824_134554	$13.41^{+5.33}_{-1.79}$	$20.53^{+13.30}_{-5.62}$	$12.19^{+5.20}_{-3.74}$	$0.60^{+0.35}_{-0.31}$	$-0.00^{+0.34}_{-0.27}$	$0.38^{+0.44}_{-0.28}$	$1.97^{+0.91}_{-1.68}$	$3.23^{+3.42}_{-1.45}$
GW230827_143829	$22.95^{+7.87}_{-5.24}$	$32.00^{+14.25}_{-8.75}$	$22.38^{+9.28}_{-7.61}$	$0.73^{+0.24}_{-0.34}$	$0.22^{+0.26}_{-0.30}$	$0.63^{+0.28}_{-0.40}$	$1.17^{+1.60}_{-0.84}$	$4.48^{+3.49}_{-2.34}$
GW230830_043238	$32.44^{+7.33}_{-5.77}$	$44.48^{+14.13}_{-10.08}$	$31.85^{+9.69}_{-9.15}$	$0.74^{+0.23}_{-0.29}$	$0.03^{+0.25}_{-0.26}$	$0.46^{+0.41}_{-0.34}$	$1.28^{+1.56}_{-0.97}$	$4.15^{+2.78}_{-1.99}$
GW230906_100145	$20.96^{+6.20}_{-4.41}$	$30.69^{+14.06}_{-9.14}$	$19.49^{+8.32}_{-6.47}$	$0.67^{+0.30}_{-0.33}$	$0.41^{+0.25}_{-0.34}$	$0.53^{+0.32}_{-0.31}$	$0.82^{+2.02}_{-0.62}$	$6.35^{+4.63}_{-3.07}$
GW231110_171731	$43.17^{+17.63}_{-8.55}$	$60.84^{+25.72}_{-15.51}$	$42.51^{+20.86}_{-14.89}$	$0.74^{+0.23}_{-0.35}$	$0.12^{+0.34}_{-0.37}$	$0.51^{+0.37}_{-0.36}$	$2.20^{+0.72}_{-1.95}$	$9.50^{+5.81}_{-5.54}$
GW231222_234123	$12.29^{+4.99}_{-1.54}$	$21.64^{+8.97}_{-6.51}$	$9.73^{+6.88}_{-2.36}$	$0.45^{+0.41}_{-0.18}$	$-0.13^{+0.46}_{-0.31}$	$0.32^{+0.38}_{-0.22}$	$1.11^{+1.63}_{-0.80}$	$2.44^{+4.68}_{-1.17}$
GW240101_061317	$17.31^{+4.63}_{-3.45}$	$25.76^{+18.51}_{-7.34}$	$15.47^{+6.81}_{-5.72}$	$0.63^{+0.33}_{-0.38}$	$0.35^{+0.32}_{-0.37}$	$0.45^{+0.36}_{-0.29}$	$0.68^{+2.11}_{-0.50}$	$4.93^{+5.38}_{-2.39}$

TABLE XII. Median and 90% credible intervals of the posteriors for up-ranked O4b candidates in GWTC-5.0. The parameters shows are the source-frame chirp mass $\mathcal{M}$, mass ratio q, the source-frame component masses m_1 and m_2, effective inspiral spin $\chi_{\rm eff}$, effective precession spin $\chi_{\rm p}$, source inclination angle θ_{JN}, and luminosity distance D_L.

Candidate	$\mathcal{M}$ $[M_\odot]$	m_1 $[M_\odot]$	m_2 $[M_\odot]$	q	$\chi_{\rm eff}$	χ_p	θ_{JN}	d_L [Gpc]
GW240426_100722	$26.48^{+10.10}_{-6.98}$	$36.66^{+18.04}_{-11.04}$	$25.81^{+11.89}_{-9.31}$	$0.73^{+0.24}_{-0.35}$	$0.08^{+0.34}_{-0.34}$	$0.49^{+0.39}_{-0.35}$	$1.98^{+0.92}_{-1.72}$	$11.26^{+8.61}_{-5.54}$
GW240426_151803	$27.48^{+10.36}_{-7.00}$	$37.52^{+19.09}_{-10.55}$	$26.91^{+11.86}_{-9.24}$	$0.74^{+0.23}_{-0.34}$	$0.03^{+0.33}_{-0.34}$	$0.48^{+0.40}_{-0.36}$	$1.06^{+1.78}_{-0.82}$	$6.84^{+6.94}_{-3.55}$
GW240430_111634	$80.83^{+23.22}_{-18.44}$	$109.17^{+35.50}_{-27.99}$	$80.61^{+30.04}_{-25.80}$	$0.77^{+0.20}_{-0.32}$	$0.15^{+0.39}_{-0.39}$	$0.52^{+0.36}_{-0.36}$	$1.24^{+1.64}_{-1.00}$	$6.81^{+4.97}_{-3.39}$
GW240629_201552	$23.01^{+5.90}_{-4.20}$	$30.98^{+10.90}_{-6.74}$	$22.99^{+7.38}_{-6.58}$	$0.76^{+0.21}_{-0.31}$	$0.07^{+0.29}_{-0.30}$	$0.48^{+0.39}_{-0.33}$	$2.25^{+0.68}_{-1.96}$	$7.08^{+4.24}_{-3.25}$
GW240828_064943	$15.68^{+16.25}_{-2.81}$	$22.01^{+32.23}_{-5.54}$	$15.25^{+12.40}_{-4.52}$	$0.70^{+0.26}_{-0.35}$	$0.24^{+0.24}_{-0.33}$	$0.46^{+0.35}_{-0.31}$	$2.18^{+0.73}_{-1.86}$	$4.37^{+12.19}_{-2.08}$
GW240828_085522	$27.91^{+7.77}_{-5.65}$	$37.73^{+14.70}_{-8.60}$	$27.78^{+9.39}_{-8.65}$	$0.76^{+0.22}_{-0.32}$	$0.07^{+0.31}_{-0.34}$	$0.51^{+0.37}_{-0.35}$	$0.95^{+1.85}_{-0.72}$	$6.55^{+4.55}_{-3.19}$
GW241129_122622	$28.28^{+10.90}_{-7.74}$	$38.87^{+18.74}_{-11.76}$	$27.56^{+13.20}_{-10.40}$	$0.74^{+0.23}_{-0.36}$	$0.04^{+0.35}_{-0.36}$	$0.52^{+0.37}_{-0.37}$	$1.99^{+0.91}_{-1.72}$	$11.36^{+8.83}_{-5.99}$
GW241219_151137	$20.41^{+5.39}_{-4.32}$	$28.70^{+10.77}_{-6.78}$	$19.84^{+6.72}_{-7.44}$	$0.71^{+0.26}_{-0.35}$	$0.19^{+0.29}_{-0.28}$	$0.46^{+0.39}_{-0.33}$	$0.88^{+1.95}_{-0.66}$	$6.38^{+4.22}_{-3.20}$